

Florida Institute of Technology

## Scholarship Repository @ Florida Tech

---

Theses and Dissertations

---

5-2020

### Nonlinear Attitude Control for a 6U CubeSat with a Flexible, Deployable Boom

Jared Walker

Follow this and additional works at: <https://repository.fit.edu/etd>



Part of the [Mechanical Engineering Commons](#)

---

Nonlinear Attitude Control for a 6U CubeSat with a Flexible, Deployable Boom

by

Jared Walker

Bachelor of Science  
Department of Mechanical Engineering  
Florida Institute of Technology  
2018

A thesis submitted to  
the College of Engineering and Science of  
Florida Institute of Technology  
in partial fulfillment of the requirements  
for the degree of

Master of Science  
in  
Mechanical Engineering

Melbourne, Florida  
May, 2020

© Copyright 2020 Jared Walker  
All Rights Reserved

---

The author grants permission to make single copies.

We the undersigned committee  
hereby approve the attached thesis

Nonlinear Attitude Control for a 6U CubeSat with a Flexible, Deployable Boom

by Jared Walker

---

Francis Bourne, Ph.D.  
Research Professor  
Aerospace, Physics and Space Sciences  
Committee Chair

---

Hector Gutierrez, Ph.D., P.E.  
Professor  
Mechanical and Civil Engineering  
Committee Member

---

Razvan Rusovici, Ph.D.  
Associate Professor  
Aerospace, Physics and Space Sciences  
Outside Committee Member

---

Ashok Pandit, Ph.D., P.E.  
Professor and Department Head  
Mechanical and Civil Engineering

## ABSTRACT

Title:

Nonlinear Attitude Control for a 6U CubeSat with a Flexible, Deployable Boom

Author:

Jared Walker

Major Advisor:

Francis Bourne, Ph.D.

A satellite attitude control system was developed in MathWork's Simulink for a 6U CubeSat with a flexible appendage payload. The flexible appendage is a boom that is able to store into a compact size and deploy out to 1 meter. The boom deploys a sensor attached to the end of the boom. The boom/sensor payload was modeled as a spring-mass-damper system. The equivalent spring constant of the payload was determined by the the natural frequency of the system. A modal analysis in ANSYS Mechanical was used to determine the natural frequencies and mode shapes of the payload. The attitude control simulation was run using environmental disturbances in low Earth orbit to excite the system. The response of the CubeSat and payload was simulated and control gains tuned to determine performance. The control system was able to hold the CubeSat to with  $\pm 0.5^\circ$  of nadir over one orbit at 400km altitude. This thesis describes the design and analysis for an attitude control system of a 6U CubeSat with a flexible appendage and sensor payload.

# Table of Contents

Abstract	iii
List of Figures	vii
List of Tables	ix
List of Symbols and Abbreviations	x
<b>Chapter 1 Introduction</b>	<b>1</b>
1.1 AddCube Mission . . . . .	1
1.2 Background Information . . . . .	2
1.3 Motivation . . . . .	3
1.4 Scope or Objectives . . . . .	4
1.5 Approach . . . . .	4
1.6 Overview . . . . .	5
<b>Chapter 2 Background</b>	<b>6</b>
2.1 Spacecraft Attitude and Dynamics . . . . .	6
2.1.1 Coordinate Frames . . . . .	7
2.1.2 Coordinate Transformations . . . . .	10
2.1.3 Kinematics . . . . .	11
2.1.4 Rigid Body Dynamics . . . . .	13
2.1.5 Orbital Dynamics . . . . .	14
2.1.6 Environmental Disturbances . . . . .	17

2.1.7	Flexible Components . . . . .	20
2.2	Structural Dynamics . . . . .	20
2.2.1	Mechanics of Materials . . . . .	21
2.2.2	Modal Analysis . . . . .	22
<b>Chapter 3</b>	<b>AddCube</b>	<b>23</b>
3.1	Mission . . . . .	23
3.2	CubeSat . . . . .	24
3.3	ADACS . . . . .	27
3.4	Deployable Boom . . . . .	27
3.5	Sensor Payload . . . . .	30
<b>Chapter 4</b>	<b>Analysis and Design Approach</b>	<b>32</b>
4.1	Attitude Control System Simulation . . . . .	32
4.1.1	Kinematics Subsystem . . . . .	32
4.1.2	Dynamics Subsystem . . . . .	34
4.1.3	Controller and Reaction Wheel Subsystems . . . . .	38
4.1.4	Orbital Environment Subsystem . . . . .	40
4.1.5	Sensor Subsystem . . . . .	42
4.2	Structural Simulations . . . . .	44
4.2.1	Modal Analysis . . . . .	44
<b>Chapter 5</b>	<b>Results</b>	<b>47</b>
5.1	Structural Simulations . . . . .	47
5.1.1	Modal Analysis . . . . .	47
5.2	Attitude Control System . . . . .	50
5.2.1	CubeSat Response . . . . .	50
5.2.2	ADACS Response . . . . .	52

5.2.3	Sensor Response . . . . .	54
5.2.4	Environmental Disturbances . . . . .	55
<b>Chapter 6</b>	<b>Conclusion</b>	<b>57</b>
6.1	Summary . . . . .	57
6.2	Discussion . . . . .	58
6.3	Future Work . . . . .	58
	References	<b>60</b>
	Appendix	<b>63</b>



# List of Figures

1.1	AddCube CAD Model . . . . .	2
1.2	Common CubeSat sizes include 1-3U, 6U, and 12U [1]. . . . .	3
2.1	Earth Centered Inertial Frame . . . . .	7
2.2	Local-Vertical Local-Horizontal Frame . . . . .	8
2.3	Roll Pitch Yaw Frame . . . . .	9
2.4	Vector in two coordinate frames with same origin [2]. . . . .	11
2.5	Kepler's Orbital Elements . . . . .	16
2.6	Solar Radiation on a Surface . . . . .	18
3.1	Pumpkin Inc SUPERNOVA Layout . . . . .	24
3.2	Solar array configuration . . . . .	25
3.3	AddCube's center of mass in the YZ plane . . . . .	26
3.4	Roccor Boom Deployer Stowed . . . . .	28
3.5	Roccor Boom Deployer in the deployed configuration . . . . .	29
3.6	Boom cross section dimensions . . . . .	29
3.7	Geometrics sensors and driver package . . . . .	30
3.8	Geometrics sensor attached to the boom bracket . . . . .	31
4.1	Top level overview of simulation . . . . .	33
4.2	Simulation kinematics subsystem . . . . .	33

4.3	Simulation dynamics subsystem . . . . .	37
4.4	Simulation PD controller subsystem . . . . .	39
4.5	simulation reaction wheel dynamics subsystem . . . . .	39
4.6	Simulation orbital environment subsystem . . . . .	40
4.7	Orbit of the CubeSat . . . . .	41
4.8	Sensor subsystem block . . . . .	43
4.9	Modal analysis setup . . . . .	45
4.10	Modal analysis generated mesh. . . . .	46
4.11	The element skewness distribution of the mesh. . . . .	46
5.1	First mode shape of the beam . . . . .	49
5.2	Second mode shape of the beam . . . . .	49
5.3	CubeSat Parameters . . . . .	51
5.4	Attitude control system response . . . . .	53
5.6	Sensor response to ACS . . . . .	55
5.7	Environmental disturbance over one orbit. . . . .	56
1	Third mode shape of the beam . . . . .	63
2	Fourth mode shape of the beam . . . . .	64
3	Fifth mode shape of the beam . . . . .	64
4	Sixth mode shape of the beam . . . . .	65

# List of Tables

2.1	Dominant environmental torques . . . . .	14
3.1	Summary of AddCube components and layout . . . . .	25
3.2	Summary of MAI-400 specifications . . . . .	27
4.1	Orbital elements used in the simulation. . . . .	41
5.1	Summary of modal frequencies and shapes . . . . .	48

# List of Symbols and Abbreviations

Symbol	Definition
$\hat{\boldsymbol{v}}$	unit vector
$\dot{\boldsymbol{v}}$	vector derivative
$\boldsymbol{v} \cdot \boldsymbol{v}$	vector dot product
$\boldsymbol{v} \times \boldsymbol{v}$	vector cross product
$\boldsymbol{C}$	rotation matrix
$\boldsymbol{\omega}$	satellite angular velocity vector [rad/s]
$\bar{\boldsymbol{q}}$	quaternion vector
$q_0$	quaternion scalar value
$\boldsymbol{q}$	full quaternion vector
$\boldsymbol{H}$	angular momentum vector [N·m·s]
$\boldsymbol{T}$	torque vector [N·m]
$\boldsymbol{I}$	moment of inertia matrix [kg·m <sup>2</sup> ]
$\boldsymbol{r}$	orbital state vector
$  \boldsymbol{v}  $	vector Euclidean norm
$\mu$	Earth's gravitational constant [km <sup>3</sup> /s <sup>2</sup> ]

Symbol	Definition
$h$	orbit angular momentum [N·m·s]
$a$	semi-major axis [km]
$e$	eccentricity
$\theta$	true anomaly [deg]
$\Omega$	right ascension of the ascending node [deg]
$i$	inclination [deg]
$\omega$	argument of perigee [deg]
$\mathbf{F}$	force vector [N]
$P$	solar momentum flux [W/m <sup>2</sup> ]
$A$	surface area [m <sup>2</sup> ]
$C_S$	coefficient of specular reflection
$C_D$	coefficient of diffuse reflection
$\hat{\mathbf{s}}$	solar radiation direction vector
$\hat{\mathbf{n}}$	body outward normal vector
$r_{cp}$	center of pressure vector [m]
$\rho$	density [kg/m <sup>3</sup> ]
$C_{DC}$	drag coefficient
$\hat{\mathbf{v}}$	orbit velocity unit vector [m/s]
$\mathbf{m}$	satellite magnetic moment [A·m <sup>2</sup> ]
$\sigma$	Stress [Pa]
$E$	Young's Modulus [Pa]
$\epsilon$	Strain
$\nu$	Poisson's Ratio
$\tau$	Shearing Stress, [Pa]

Symbol	Definition
$\gamma$	Shearing Strain
G	Modulus of Rigidity [Pa]
$m$ ( $[M]$ )	Mass (Mass Matrix) [kg]
$k$ ( $[K]$ )	Spring Constant (Spring Matrix) [N/m]
$\{D\}$	Node Vector

*Abbreviations*

ECI	Earth Centered Inertial Frame
ECEF	Earth Centered Earth Frame
LVLH	Local Vertical Local Horizontal Frame
ORB	Perifocal Orbital Frame
RPY	Roll Pitch Yaw Frame
BFF	Body Fixed Frame
LEO	Low Earth Orbit
GEO	Geosynchronous Equatorial Orbit
SC	Spacecraft
RW	Reaction Wheels

# Chapter 1

## Introduction

### 1.1 AddCube Mission

The AddCube mission, sponsored by L3Harris (formerly Harris Corp,) will develop innovative technologies intended for use on CubeSats. Various technologies have been proposed such as 3D printing, slit-tube deployable booms, and precision magnetometers [3]. The common theme among the majority of missions and technologies considered is the need to deploy or create a boom meters in length from within the confines of a 6U CubeSat. These booms would be made of carbon composite or thermoplastic material with thin cross sections and would be considered flexible appendages. While flexible appendages are not new to the space industry as they have been included on many missions usually to move a magnetometer away from the spacecraft, they are a newcomer to the Small-Sat market. This paper looks to design a control system for a 6U CubeSat with a flexible boom that is deployed while on orbit.

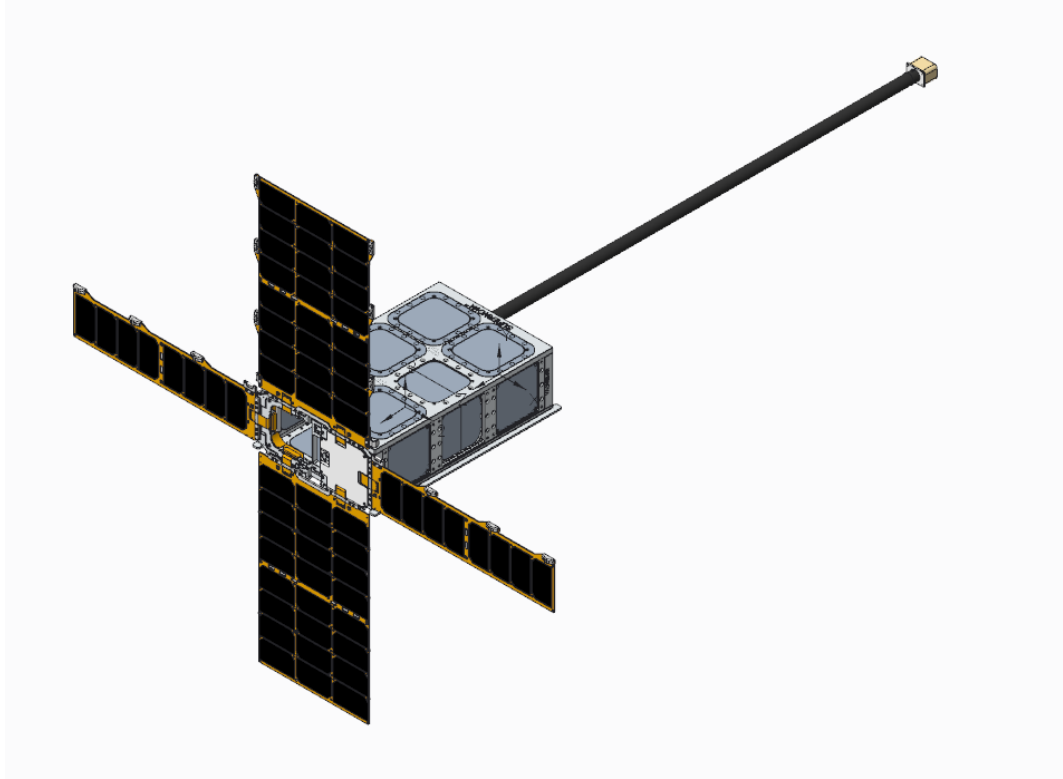


Figure 1.1: The AddCube CAD Model shows the boom extending out the -Z-axis with the sensor and sensor bracket.

## 1.2 Background Information

A CubeSat is a type of SmallSat that adheres to the CubeSat standard form-factor. The form-factor defines a unit, 1U, to be a  $10 \times 10 \times 10 \text{ cm}^3$  cube [4]. A satellite can be made up of multiple U's. Typical configurations for CubeSats are 1U, 3U, and 6U with other larger configurations of 12U and 27U becoming more common in recent years [1]. Initially, CubeSats were designed to enable low cost satellite missions that were focused on university science and education. In recent years, commercial interests have begun to consider CubeSats as an alternative ... Since the program launch in 1999, there have been over 1200 CubeSats missions proposals and launches [5]. From 2013–2016 alone, about 500 CubeSats were



launched successfully [6]. There have even been a few rocket providers developing a rocket dedicated to the Small-Sat market. This has been motivating the expansion of research and technology development to push the limits of what CubeSats and other small satellites can do.

Most missions consider the satellite to be a rigid body where any motion of the spacecraft occurs equal across all point on the spacecraft. Having a flexible component can have serious effects when the natural frequencies of the flexible component as the rigid body modes or the control system response [7].

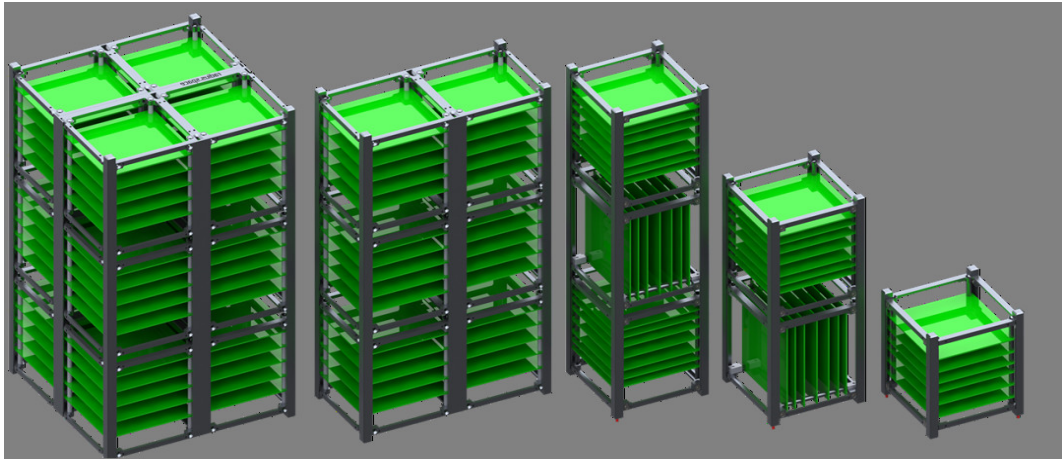


Figure 1.2: Common CubeSat sizes include 1-3U, 6U, and 12U [1].

## 1.3 Motivation

The SmallSat industry is focused on achieving low-cost missions that expand the boundaries of what is possible in small and lightweight form factors [8]. In all areas from structures to payloads, designers are looking to minimize the cost of size and weight and maximize performance and function. Several companies are looking to push the boundaries of deployable structures by designing them to store down into

small form factors. Rocco, AstroTube, and Composite Technology Development (CTD) are all developing flexible composite booms from 1m to 5m in length which are able to retract into volumes that fit well within 1U including mechanisms and housing [9]. This includes sensors that might require separation such as a gravity gradiometers or magnetometers. Remote sensors with fine attitude control can enable high accuracy measurement of Earth's gravity and magnetic field [10]. For this paper, a magnetometer is assumed to be attached at the free end of the boom.

## **1.4 Scope or Objectives**

The objective of this research was to determine the impact of a flexible boom dynamics on the CubeSat's attitude control system (ACS). This paper focuses on attitude control while the boom has been deployed and operational therefore de-tumbling is not considered. The CubeSat will be subjected to external environmental disturbances found in Low Earth Orbit (LEO).

## **1.5 Approach**

The CubeSat is modeled as a rigid body with a flexible boom. This is considered to be a hub-mast system in the current literature. The solar arrays are not considered to be flexible. An attitude control system is developed using Mathworks Simulink program. Simulink was chosen to its ease of use, robust toolboxes, and its ubiquity in control systems.

## 1.6 Overview

The present chapter presents the overview of the mission and provides relevant background information on the industry and current literature. Chapter 2 details the theory and mathematics of attitude control. Chapter 3 details the analysis and subsequent design of the attitude control system. Chapter 4 presents the results of the attitude simulation. Chapter 5 summarizes the results of the research and presents recommendations for future work to refine and test the accuracy of the research.

# Chapter 2

## Background

### 2.1 Spacecraft Attitude and Dynamics

The following section describes important concepts in attitude dynamics, kinematics, and control theory used in the research. These concepts include various coordinate frames Extensive use of coordinate frames is used so it is presented first. The spacecraft's change in attitude is presented in the kinematics section and the angular rates of the CubeSat is presented in the dynamics sections. The orbital dynamics of the spacecraft is introduced and the environmental disturbances the CubeSat will experience is presented. Finally, some background is presented on the introduction of flexible components and how it impacts the performance of the spacecraft's attitude control system.

### 2.1.1 Coordinate Frames

It is important to define various reference frames when working with relative motion of two objects. Three types of coordinate frames which are particularly useful for orbiting satellites are inertial frames, orbital frames, and body-fixed coordinate frames. The frames used in the research are described below. Each coordinate frame has advantages and disadvantages and moving from one frame to another must be taken carefully.

#### Earth Centered Inertial Frame

The typical inertial frame used in satellite attitude models is Earth Centered Inertial (ECI) frame. The coordinate system has the origin at the center of the Earth where the z-axis points in the direction of true North, the x-axis points in the direction of the vernal equinox, and the y-axis completes the right-hand orthogonality rule. While this is not a truly inertial frame as it precesses over a long period of time, in the case of most satellites it can be considered inertial.

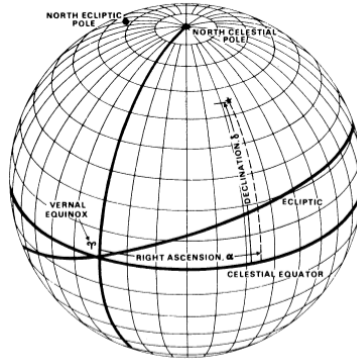


Figure 2.1: Earth Centered Inertial Frame points to the vernal equinox along the x-direction [7].

## Earth-Centered Earth-Fixed Frame

Another common reference frame is Earth Centered Earth Fixed which is similar to the ECI frame except it is non-inertial as it is fixed to the Earth. The z-axis are co-aligned in the ECI and ECEF frame, but the x-axis in ECEF frame points to the Prime Meridian, and again the y-axis completes the right-hand rule. The ECEF frame is typically used for geolocation and determining the magnetic field vector at the satellite's position.

## Local-Vertical Local-Horizontal Frame

The Local-Vertical Local-Horizontal frame (LVLH), also known as East North Zenith (ENZ), is a non-inertial frame with the origin located along the orbital path. The x-axis points outward from the center of the Earth, the y-axis points East (increasing longitude), and the z-axis completes the right-hand rule and is pointing towards North (increasing latitude) as seen in Figure 2.2.

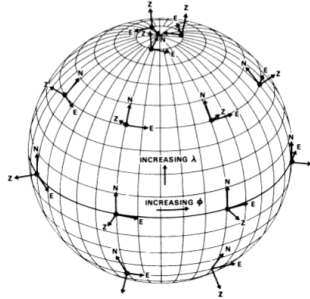


Figure 2.2: The Local-Vertical Local-Horizontal Frame, also known as East North Zenith, is a non-inertial frame that is dependent on the longitude and latitude of the satellite [7].

## Roll, Pitch, Yaw Frame

The roll pitch yaw (RPY) frame is a common frame of reference for nadir pointing spacecraft as one axis is always pointing towards the center of the Earth. The RPY frame is an orbital frame where the roll axis (x-direction) is along the velocity tangent of the orbit, the yaw axis (z-direction) points towards the center of the earth, and the pitch axis (y-direction) points normal to the orbital plane as seen in Figure 2.3.

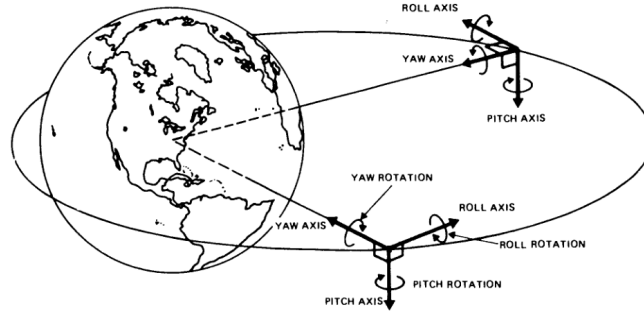


Figure 2.3: Roll pitch yaw frame is an orbital frame the rotates about the pitch axis [7].

## Body-Fixed Frame

The body-fixed or spacecraft-fixed coordinate system is a user defined frame that is fixed on the spacecraft. This coordinate system places its origin at the spacecraft's center of mass (COM) and follows the right-hand rule for the user's defined orientation. The coordinate axes can aligned with the spacecraft's principal axes using a coordinate transformation which uncouples the equations of motion. The body-fixed frame used has the x-axis normal to the 3U side, y-axis normal to the 6U side, and the z-axis normal to the 2U side as shown in Figure 1.1.

### 2.1.2 Coordinate Transformations

One frequently moves between reference frames when analyzing and evaluating issues related to spacecraft attitude control since disturbances, pointing, and dynamics is typically analyzed in their relevant coordinate frames. Such as the magnetic field is expressed in the ECEF or LVLH frame whereas the satellite dynamics are expressed in the ECI frame. To transform a vector in one coordinate system to another a rotation matrix, also known as a direction cosines matrix, is used. A vector can be described using two coordinate frames shown in Figure 2.4. For example, the spacecraft's attitude might be in body-fixed coordinates with respect to the RPY frame and need to be transformed to body-fixed with respect to the ECI frame. That vector defined in one frame,  $\mathbf{r}_1$  can be expressed in another frame,  $\mathbf{r}_2$  by using a rotation matrix,  $\mathbf{C}_{12}$  as shown

$$\mathbf{r}_1 = \mathbf{C}_{12}\mathbf{r}_2 \quad (2.1)$$

The simplest rotation matrices which is a rotation about one of the Cartesian axis is given by Equations 2.2, 2.3, and 2.4. These rotations can be combined to fully describe the orientation of one reference frame to another.

$$\mathbf{C}_x = \begin{bmatrix} 1 & 0 & 0 \\ 0 & \cos(\theta) & \sin(\theta) \\ 0 & -\sin(\theta) & \cos(\theta) \end{bmatrix} \quad (2.2)$$

$$\mathbf{C}_y = \begin{bmatrix} \cos(\theta) & 0 & -\sin(\theta) \\ 0 & 1 & 0 \\ \sin(\theta) & 0 & \cos(\theta) \end{bmatrix} \quad (2.3)$$



$$\mathbf{C}_z = \begin{bmatrix} \cos(\theta) & \sin(\theta) & 0 \\ -\sin(\theta) & \cos(\theta) & 0 \\ 0 & 0 & 1 \end{bmatrix} \quad (2.4)$$

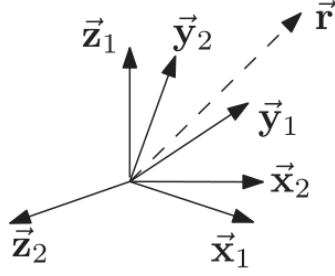


Figure 2.4: Vector in two coordinate frames with same origin [2].

### 2.1.3 Kinematics

Kinematics is the study of a rigid-body motion without considering the forces that cause them to move. Rotational kinematics describes the orientation of a body that is in rotational motion.

#### Euler Angles

One common method to parameterize the spacecraft's attitude is 3 successive principal rotations to describe the orientation of the satellite with respect to another frame. The order of the rotations is arbitrary as long as the order is preserved throughout. There are 12 possible combinations of rotations which can be divided into two types. The first type incorporates rotations about each axis and has a singularity when  $\theta = \pm 90$  deg. The second type repeats a rotation about an axis but not in successive rotations and has a singularity at  $\theta = 0$  deg and 180 deg. A

common choice in rotation sequence is 3-2-1 which is a rotation about the z-axis then a rotation about the intermediate y-axis and finally a rotation about the transformed x-axis which the direction cosines matrix is given by Eq. 2.5.

$$\begin{aligned} \mathbf{C}_{3-2-1}(\phi, \theta, \psi) &= \mathbf{C}_x(\phi)\mathbf{C}_y(\theta)\mathbf{C}_z(\psi) \\ &= \begin{bmatrix} c(\theta)c(\psi) & c(\theta)s(\psi) & -s(\theta) \\ s(\phi)s(\theta)c(\psi) - c(\phi)s(\psi) & s(\phi)s(\theta)s(\psi) + c(\phi)c(\psi) & s(\phi)c(\theta) \\ c(\phi)s(\theta)c(\psi) + s(\phi)s(\psi) & c(\phi)s(\theta)s(\psi) - s(\phi)c(\psi) & c(\phi)c(\theta) \end{bmatrix} \end{aligned} \quad (2.5)$$

where  $c(a) = \cos(a)$  and  $s(a) = \sin(a)$ . The kinematic equation in Euler angles for the rigid-body spacecraft's attitude is given by:

$$\begin{bmatrix} \dot{\phi} \\ \dot{\theta} \\ \dot{\psi} \end{bmatrix} = \begin{bmatrix} 1 & \sin(\phi) \tan(\theta) & \cos(\phi) \tan(\theta) \\ 0 & \cos(\phi) & -\sin(\phi) \\ 0 & \sin(\phi) \sec(\theta) & \cos(\phi) \sec(\theta) \end{bmatrix} \boldsymbol{\omega} \quad (2.6)$$

## Quaternion

Quaternions can be used as an alternative to Euler angles. They have the advantage of avoiding the singularities associated with Euler angle sequences. Quaternions add an additional parameter, a scalar, to the vector. Another advantage of using quaternions is computational efficiency since the equations of motion are then purely algebraic and do not contain any trigonometric functions. The kinematic equations for the quaternion representation of attitude is defined by Eq. 2.7:

$$\dot{\bar{\mathbf{q}}} = \frac{1}{2} (q_0 \boldsymbol{\omega} - \boldsymbol{\omega} \times \bar{\mathbf{q}}) \quad (2.7a)$$

$$\dot{q}_0 = -\frac{1}{2} \boldsymbol{\omega}^T \bar{\mathbf{q}} \quad (2.7b)$$

where the vector part is  $\bar{\mathbf{q}} = [q_1 \ q_2 \ q_3]^T$ . Quaternion can also be represented using one vector that includes the vector and scalar portion as shown by  $\mathbf{q} = [q_0 \ q_1 \ q_2 \ q_3]^T$ . Different notations of quaternions include  $\mathbf{q} = [q_1 \ q_2 \ q_3 \ q_4]^T$  and  $\mathbf{q} = [q_w \ q_x \ q_y \ q_z]^T$  where  $q_4$  and  $q_w$  are the scalar values. The notation in Eq. 2.7 will be used throughout this paper.

#### 2.1.4 Rigid Body Dynamics

Dynamics is the study of motion and the forces affecting motion. In this study, the spacecraft is assumed to be a rigid body meaning that there is no deformation of any particle of the spacecraft with respect to any other particle. Therefore, the motion of the spacecraft is a superposition of a translation (orbital dynamics) and a rotation (attitude dynamics). The change of angular momentum of the satellite is equal to the external torque applied about the center of mass of the rigid body, as shown in Equation 2.8,

$$\dot{\mathbf{H}} = \mathbf{T}_{ext} \quad (2.8)$$

where the angular momentum is the product of the moment of inertia and the angular velocity of the rigid body

$$\mathbf{H} = \mathbf{I} \boldsymbol{\omega} \quad (2.9)$$

Combining Eq. 2.8 and 2.9 yields the equations of angular motion of the spacecraft in body-fixed frame with respect to the inertial frame, as shown in Eq. 2.8.

$$\mathbf{I}\dot{\boldsymbol{\omega}} = \mathbf{T}_{ext} - \boldsymbol{\omega} \times \mathbf{I}\boldsymbol{\omega} \quad (2.10)$$

### 2.1.5 Orbital Dynamics

Orbital dynamics does not have any effect on the spacecraft's attitude or dynamics directly but does determine the magnitude of external disturbances the spacecraft will encounter. For example, the dominant disturbances for satellites in LEO are aerodynamic drag and gravity gradient where for satellites in GEO it will be solar radiation pressure and gravity gradient [11]. The general spheres of influence is summarized in Table 2.1. The relative motion of an object orbiting about a mass is given by the two-body equation which can be written in the state vector form

$$\ddot{\mathbf{r}} = -\frac{\mu}{\|\mathbf{r}\|^3}\mathbf{r} \quad (2.11)$$

where  $\mathbf{r}$  is the vector from the center of the Earth to the center of the orbiting body given in ECI coordinates and  $\mu$  is the gravitational constant for Earth which is  $3.986 \times 10^5 \text{ km}^3/\text{s}^2$ . The position and velocity can be found by solving this differential equation.

Table 2.1: Dominant environmental torques for various altitudes of a satellite.

Altitude, km	Dominate Environmental Disturbance
< 300	Aerodynamic drag
300 – 650	Aerodynamic drag and gravity gradient
650 – 100	Aerodynamic drag solar pressure and gravity gradient
> 1000	Solar pressure and gravity gradient

The classical orbital elements or Keplerian elements are a six parameter set that uniquely determine an orbit and the position on the orbit in an inertial frame. Two parameters, the semi-major axis,  $a$  and the eccentricity,  $e$ , defines the orbit shape and size within the orbital plane. Three additional parameters define the orbit in three-dimensions. Three rotation angles, inclination,  $i$ , right ascension of the ascending node,  $\Omega$ , and argument of periapsis,  $\omega$ , can be used to define the orientation of the orbital plane with respect to an inertial frame [12]. The inclination is the angle of tilt the orbital plane has with respect to the equatorial plane where the right ascension of the ascending node is the angle between the vernal equinox and where the satellite intersects the equatorial plane. The argument of periapsis is the angle from the ascending node to perigee. For a circular orbit, the argument of perigee is arbitrary since there is no perigee point. The last element, true anomaly, is used to define the position of the satellite along the orbit. All six classical elements are illustrated in Figure 2.5. Classical orbital elements can be transformed into orbital state vectors to be used in Equation 2.11 by first computing the state vectors in the orbital frame and using a Euler rotation sequence using the three angle parameters. The angular momentum of the orbit is determined by

$$h = \sqrt{\mu a(1 - e^2)} \quad (2.12)$$

The position vector in the orbital frame can be found using Equation 2.13 and the corresponding velocity vector can be found using Equation 2.14.

$$\mathbf{r}^{orb} = \frac{h^2/\mu}{1 + e \cos \theta} \begin{bmatrix} \cos \theta \\ \sin \theta \\ 0 \end{bmatrix} \quad (2.13)$$

$$\dot{\mathbf{r}}^{orb} = \frac{\mu}{h} \begin{bmatrix} \sin \theta \\ e + \cos \theta \\ 0 \end{bmatrix} \quad (2.14)$$

The transformation of the position and velocity vectors from orbital to inertial frame is a 3-1-3 Euler rotation sequence given by Equation 2.15. The position and velocity state vectors are found by the product of the rotation matrix and the state vector in the orbital frame, as seen in Equations 2.16 and 2.17.

$$\mathbf{C}^{eci/orb} = \mathbf{C}_3^T(\Omega) \mathbf{C}_1^T(i) \mathbf{C}_3^T(\omega) \quad (2.15)$$

$$\mathbf{r}^{eci} = \mathbf{C}^{eci/orb} \mathbf{r}^{orb} \quad (2.16)$$

$$\dot{\mathbf{r}}^{eci} = \mathbf{C}^{eci/orb} \dot{\mathbf{r}}^{orb} \quad (2.17)$$

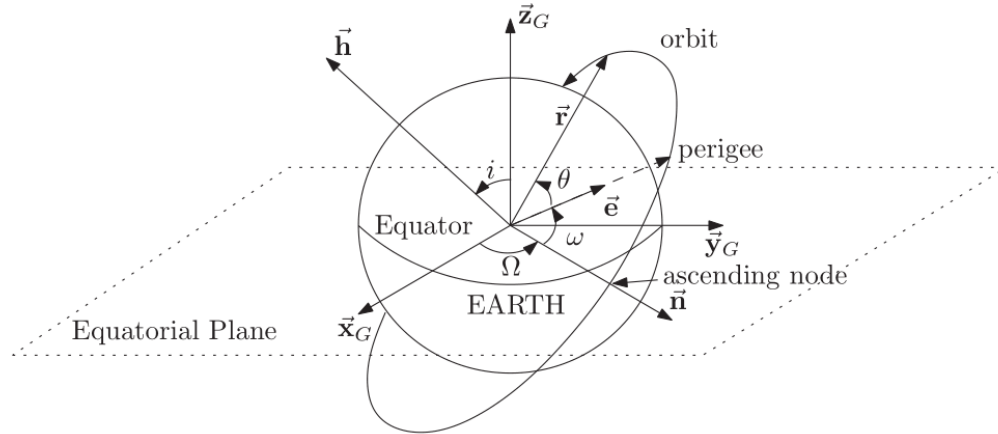


Figure 2.5: Kepler's orbital elements describes the location of a satellite with respect to inertial coordinates [2].

### 2.1.6 Environmental Disturbances

The external torques acting on the satellite include the gravity gradient, solar radiation pressure, aerodynamic drag, and magnetic disturbance due to the magnetorquers (magnetic field of the spacecraft or payload due to hysteresis or others are not included in this thesis).

#### Gravity Gradient

The gravity gradient torque is due to inverse square gravitational field which causes a variation of force over the satellite. A useful method to calculate this torque is to use the mass moment of inertia of the satellite in body coordinates. The gravity gradient torque is normal to the local vertical coordinate and is inversely proportional to the cube of the distance to the center of Earth.

$$\mathbf{T}_{grav} = -\frac{3\mu}{||\mathbf{r}||^3} (\hat{\mathbf{r}} \times \mathbf{I}\hat{\mathbf{r}}) \quad (2.18)$$

where  $\hat{\mathbf{r}}$  is the unit vector for the inertial position in body-fixed coordinates.

#### Solar Radiation Pressure

A torque can be produced by solar radiation pressure when the center of pressure from the incident radiation is not aligned with the center of mass. The solar radiation pressure is caused by incident solar radiation on the surface of the satellite. The intensity of the pressure is determined by the satellite's radiative properties, geometry, and the position and orientation in relation to the Sun and Earth's

umbra. The solar radiation pressure force is given by Equation 2.19.

$$\mathbf{F}_{solar} = -PA \cos \theta \left[ (1 - C_S) \hat{\mathbf{s}} + 2(C_S \cos \theta + \frac{1}{3}C_D) \hat{\mathbf{n}} \right] \quad (2.19)$$

where  $P$  is the solar flux constant,  $\cos(\theta) = \hat{\mathbf{s}} \cdot \hat{\mathbf{n}}$ ,  $C_s$  is the specular radiation coefficient, and  $C_D$  is the diffuse radiation coefficient. Then the torque is given by the cross product of the force vector and the vector from the center of mass to the center of pressure.

$$\mathbf{T}_{solar} = \mathbf{r}_{cp} \times \mathbf{F}_{solar} \quad (2.20)$$

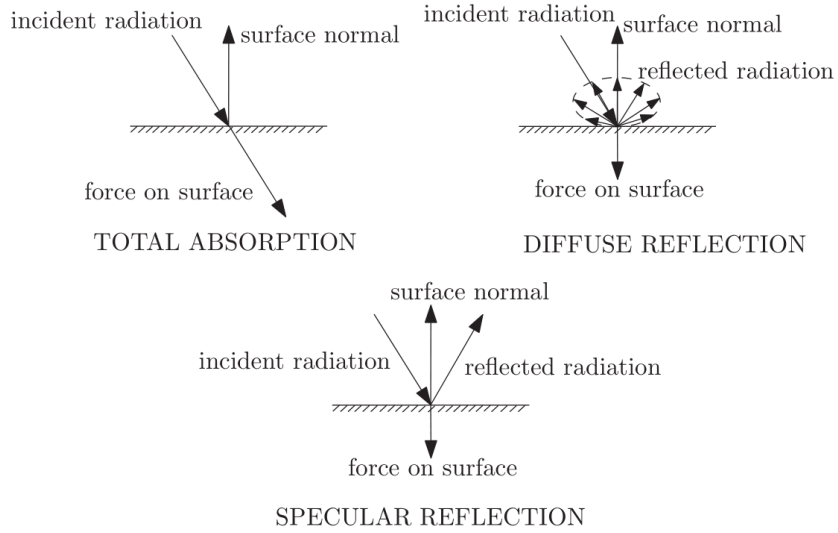


Figure 2.6: Incident radiation on a surface can be reflected or absorbed.

## Aerodynamic Drag

Even in low orbit the spacecraft will still experience drag due to Earth's atmosphere. The drag is directed in the opposite direction of the orbital velocity vector. It is a function of the area that the velocity vector passes through, the coefficient of



drag, and speed of the satellite, and atmospheric density. The aerodynamic drag force is given by:

$$\mathbf{F}_{aero} = \frac{1}{2} \rho C_{DC} A V^2 (\hat{\mathbf{n}} \cdot \hat{\mathbf{v}}) \hat{\mathbf{v}} \quad (2.21)$$

where  $\hat{\mathbf{v}}$  is the velocity vector in body coordinates,  $\hat{\mathbf{n}}$  is the outward normal of the surface,  $\rho$  is Earth's atmospheric density at the altitude, and  $C_{DC}$  is the coefficient of drag. A torque center of mass is produced when the resultant center of pressure where the aerodynamic force is applied is not coincident with the center of mass. The aerodynamic torque about the center of mass is given by:

$$\mathbf{T}_{aero} = \mathbf{r}_{cp} \times \mathbf{F}_{aero} \quad (2.22)$$

## Magnetic Disturbance

The magnetic disturbance stems from the interaction between the spacecraft's residual magnetic field and the earth's magnetic field. The magnetic disturbance is only considered for the magnetorquers and not residual field of the spacecraft and its components.

$$\mathbf{T}_{mag} = \mathbf{m} \times \mathbf{B}_E \quad (2.23)$$

where  $\mathbf{m}$  is the satellite's magnetic dipole moment and  $\mathbf{B}_E$  is the Earth's magnetic field strength vector. Two detailed models of the Earth's magnetic field are readily available, the International Geomagnetic Reference Field (IGRF) and the World Magnetic Model (WMM). The IGRF model is a 13th order and degree spherical harmonics model. The WMM consists of a 12th order and degree spher-

ical harmonic field model. MathWorks includes Simulink blocks for both models, however, using the WMM model with updated coefficients caused issues in the model so the IGRF model was used.

### **2.1.7 Flexible Components**

Flexible body dynamics can have a significant impact on the overall dynamics of the spacecraft when the natural frequencies of the flexible component are of the same magnitude as the control system bandwidth. When they are of similar magnitudes, the flexible component could be easily excited by the actuation of the control system. Flexible components can be modeled in several ways. The flexible component response may be modeled as an external disturbance or included in the dynamics of the entire spacecraft. To include the motion of the flexible components and their impact on the ADACS performance and stability, additional degrees of freedom must be incorporated into the model. These degrees of freedom are coupled with the rigid body motion of the spacecraft. The coupled equations of motion must be solved simultaneously to include all effects of the flexibility modeled.

## **2.2 Structural Dynamics**

This section introduces concepts about mechanics of materials and structural dynamics that was used in the modeling and analysis of the composite boom. Material properties and its relations to stress and strain are presented in the first section. In addition, the concept of modal analysis and its application in finite element models is introduced.

### 2.2.1 Mechanics of Materials

Material properties are important for the structural analysis of the payload. The beam is made out of a hybrid carbon and glass composite made by Roccort which is an orthotropic material. The relationship between stress and strain is given by Hooke's Law which states that the stress,  $\sigma$  is directly proportional to the strain,  $\epsilon$ :

$$\sigma = E\epsilon \quad (2.24)$$

where  $E$  is the Young's modulus or modulus of elasticity. Another important material property is Poisson's ratio. Poisson's ratio is the relationship between the lateral and axial strain. For a material under normal stress, it will undergo contractions in the transverse directions. It is determined by Equation 2.25.

$$\nu = \frac{\epsilon_{lateral}}{\epsilon_{axial}} \quad (2.25)$$

If a material is under general stress, shearing stress might be present. The relationship between shearing stress,  $\tau$  and shearing strain,  $\gamma$  is given by Hooke's law for shearing stress and strain:

$$\tau_{xy} = G_{xy}\gamma_{xy} \quad (2.26)$$

where  $G$  is the modulus of rigidity.

For an orthotropic material, there are different moduli of elasticity, rigidity, and Poisson's ratio for each direction of the stress. Laminates will typically have their material properties of the fibers and matrix combined into equivalent homogeneous

properties. For an orthotropic material subjected to multi-axial loads, the above relationships can be combined to form the generalized Hooke's Law:

$$\epsilon_x = +\frac{\sigma_x}{E_x} - \frac{\nu_{yx}\sigma_y}{E_y} - \frac{\nu_{zx}\sigma_z}{E_z} \quad (2.27a)$$

$$\epsilon_y = -\frac{\nu_{xy}\sigma_x}{E_x} + \frac{\sigma_y}{E_y} - \frac{\nu_{zy}\sigma_z}{E_z} \quad (2.27b)$$

$$\epsilon_z = -\frac{\nu_{xz}\sigma_x}{E_x} - \frac{\nu_{yz}\sigma_y}{E_y} + \frac{\sigma_z}{E_z} \quad (2.27c)$$

### 2.2.2 Modal Analysis

A modal analysis is the solution to the undamped, free vibration equation of motion which in matrix form is shown in Equation 2.28. From the solution, the mode shape and corresponding natural frequencies of the system can be found. Only the stiffness and the mass need to be known for the system to calculate the natural frequencies and mode shapes. There are various methods of solving this equation for discrete systems. This includes the exact method which involves the eigenvalue problem and other methods such as the Rayleigh-Ritz Method and Dunkerley Formula [13]. These methods will not be described in this thesis. Instead an overview of modal performed for discrete systems will be presented. The software used to determine the natural frequencies is ANSYS Mechanical which uses the Block-Lanczos iteration method to find the eigenvalues [14].

$$[M]\{\ddot{D}\} + [K]\{D\} = 0 \quad (2.28)$$

# Chapter 3

## AddCube

### 3.1 Mission

One alternative being considered for the AddCube mission is to measure the magnetic field on orbit which requires stable pointing and low magnetic interference around the sensor. By moving the magnetometer sensor away from the spacecraft by using a boom, it reduces the magnetic interference from the spacecraft. Since the CubeSat is relatively small a deployable boom is ideal to store in a compact size. Therefore, AddCube utilizes a 6U chassis and a deployable boom to move the sensor out 1m.

## 3.2 CubeSat

AddCube uses Pumpkin Inc. 6U SUPERNOVA chassis along with their solar array and electronics stack. The SUPERNOVA chassis has an allowable internal volume of 7000cc and allows for 14kg total mass including the payload. The chassis is made from 6061 and anodized 7071 aluminum and has a mass of 1.64kg. Figure 3.2 shows the solar array configuration which includes 2x3U and 2x6U solar panels [15]. The electronics stack consists of six printed circuit board (PCB) modules and other hardware [16]. The electronics stack takes up 1U of volume and is located in A1 as seen in Figure 3.1. The battery module and ADACS is located in A2 has a combined mass of 1,374g.

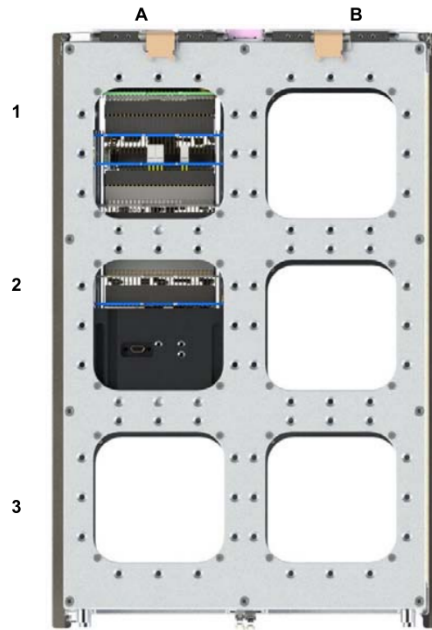


Figure 3.1: Pumpkin Inc SUPERNOVA layout specified the location for the bus stack and allowable location for the payloads [17].

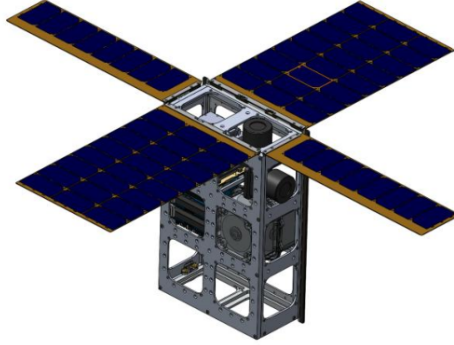


Figure 3.2: The solar array include 2x3U and 2x6U solar panels that orient in the z-direction when deployed [17].

Table 3.1: Summary of AddCube components and their volume requirements, mass, and location within the chassis.

Component	Volume Required	Mass	Location
Chassis	-	1640g	-
Electronics Stack	1U	400g	A1
Battery Module	1/2U	680g	A2
ADACS	1/2U	694g	A2
Solar Array	-	1020g	-
Communications	1/2U	138g	A3 or B3
Deployer	1/2U	250g	B2
Sensor Driver	1/2U	200g	A3 or B3
Sensor+Bracket	1/2U	40g	B3

Most of the mass is concentrated close to the center of geometry for the Cube-Sat. The heaviest components, the ADACS and battery module, is located in the center of the z-axis and y-axis. It is offset from the x-axis by 5cm (1/2U). The solar array shifts the center of mass in the z-axis. This configuration makes the moment of inertia matrix close to a diagonal matrix. The moment of inertia matrix was determined in Creo Parametric assuming all components center of mass occurred at their respective center of geometry. The mass of component was converted to a equivalent density by its volume in Creo. The center of mass of the CubeSat can be seen in Figure 3.3. The matrix for the moment of inertia determined by Creo Parametric was

$$\mathbf{I}_{sc} = \begin{bmatrix} 1.1345441e-1 & -6.6281550e-5 & -3.6679218e-3 \\ -6.6281550e-5 & 1.6171740e-1 & -5.2440383e-4 \\ -3.6679218e-3 & -5.2440383e-4 & 6.2754346e-2 \end{bmatrix} \quad (3.1)$$

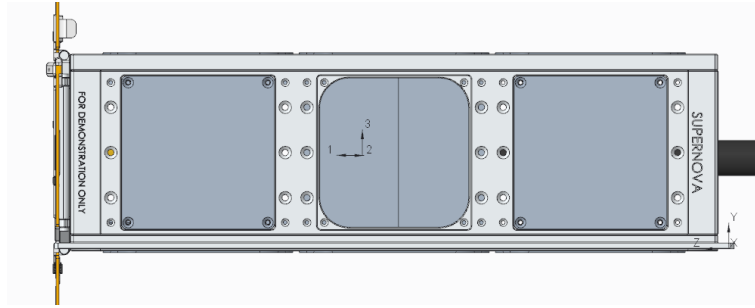


Figure 3.3: AddCube's center of mass as seen in the XZ plane shows the center of mass shifted towards the solar array.



### 3.3 ADACS

The Attitude Determination and Control System (ADACS) uses the MAI-400 from Maryland Aerospace Inc. The ADACS is 1/2U in volume and has a mass of 694 grams. The ADACS includes three reaction wheels, two IR Earth horizon sensors, three electromagnets, and the controller. The MAI-400 can provide a max torque of 0.635 mN·m with a maximum of 9.351 mN·m·s momentum storage [18]. A summary of the MAI-400 specifications is found in Table 3.2. the MAI-400 is attached to the electronics stack and is located in A2.

Table 3.2: Summary of MAI-400 specifications

<b>Spec</b>	<b>Value</b>	<b>Unit</b>
Mass	694	g
Volume	1/2	U
Max Torque	0.635	mN·m
Max Storage	9.351	mN·m·s
Max RW Speed	10,000	RPM
Max Dipole Moment	0.108	A·m <sup>2</sup>

### 3.4 Deployable Boom

L3Harris suggested Rocco as the developer for the boom due to their expertise and flight records in composites and deployables for the SmallSat market. They developed a 1/2U deployable boom for NASA's Goddard and Air Force Research Laboratory on deployable instrument booms. Their strain-driven magnetometer boom is scheduled on upcoming NASA missions [19]. A motor driven deployer is in development as well. The deployable boom is made from a hybrid carbon-glass or all carbon composite that is formed in the shape of a split tube. This shape allows the boom to be rolled up into a compact volume much like a tape measure

as seen in Figures 3.4 and 3.5. This allows for a relatively long length for a beam to be included in a CubeSat or other SmallSat. The orthotropic laminate has a thickness of 0.23mm. The largest modulus of elasticity and modulus of rigidity is in the axial direction of the boom. For the purpose of this study, the boom was modeled as a surface model in Creo Parametric with a length of 1m and a nominal diameter of 20mm. The angle between the two ends of the arc cross section is  $30^\circ$  and is shown in Figure 3.6.

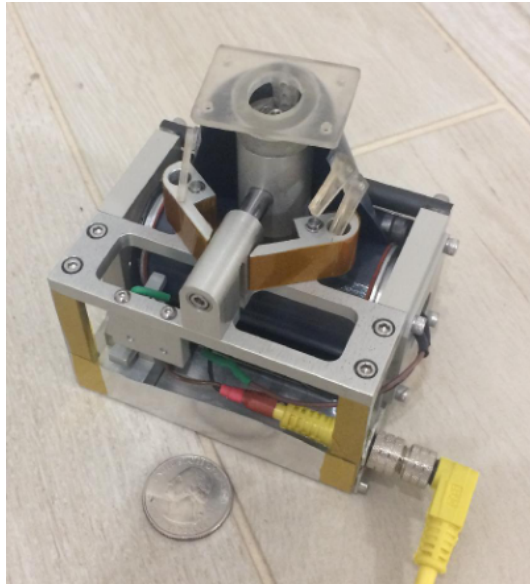


Figure 3.4: Rocco Boom Deployer in the stowed configuration.



Figure 3.5: Roccoor Boom Deployer in the deployed configuration

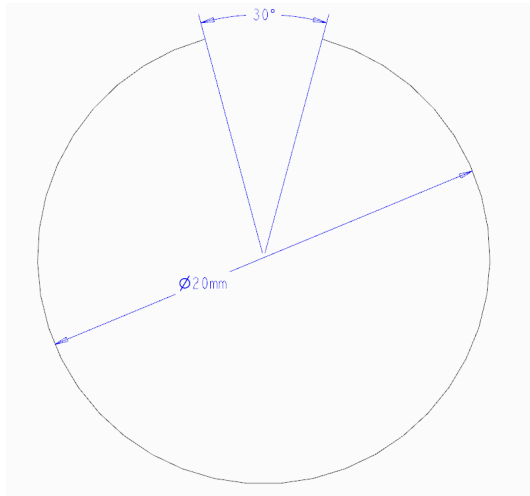


Figure 3.6: The boom has a nominal diameter of 20mm and a subtended angle of  $30^\circ$ .

### 3.5 Sensor Payload

A sensor is attached to the free end of the deployable boom. Geometrics was selected as a typical supplier of the sensor of interest in this study. They produce magnetometers and seismographs for airborne, marine, and land applications. They are developing a microelectromechanical (MEMS) magnetometer with small size and mass that would be suitable for use in a CubeSat. The Geometrics magnetometer consists of two sensor modules, each has a mass of 30 grams and a driver module which has a mass of 250 grams [20]. The Geometrics components is shown in Figure 3.7. One of the sensor modules will be attached to the boom using the boom payload bracket. The sensor bracket was modeled using Creo Parametric and can be seen in Figure 3.8. The bracket provides an interface between the boom and sensor. The bracket also provides torsional stiffness in the boom since the open cross section of the free end is constrained to the bracket. The bracket and sensor assembly can be treated as rigid bodies with respect to the boom.

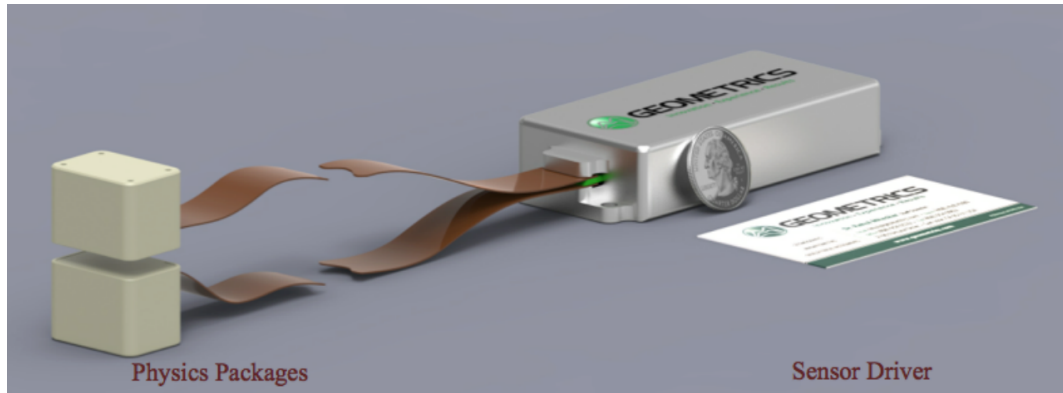


Figure 3.7: Geometrics magnetometer package includes two sensors and one driver module [20].

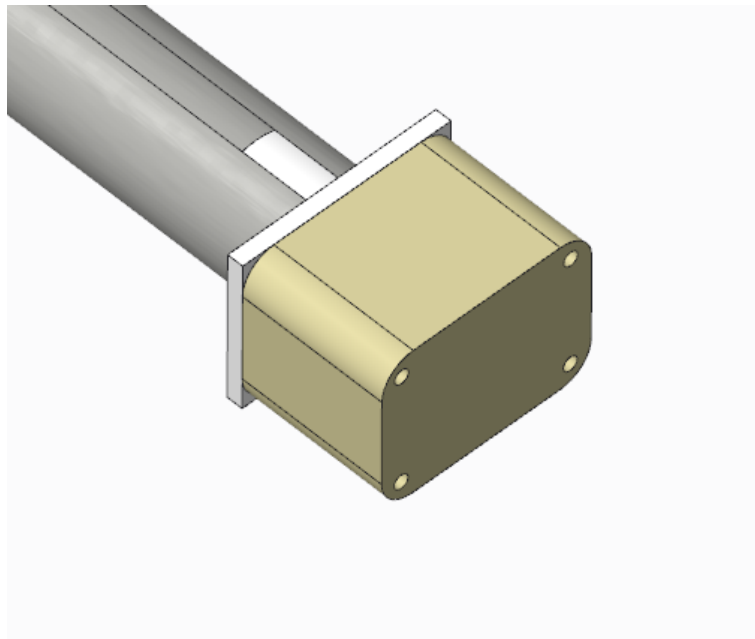


Figure 3.8: Geometrics magnetometer sensor is attached using a bracket that is fixed to the boom.

# Chapter 4

## Analysis and Design Approach

### 4.1 Attitude Control System Simulation

The attitude control system simulation was modeled in Simulink using MATLAB 2019b. The simulation consists of several subsystems for organization as well as to improve readability and debugging of the model. The top level of the simulation presents the configuration of the satellite and other parameters and can be seen in Figure 4.1. Here the user can input orbital elements, moment of inertia matrix as well as the initial conditions of the CubeSat. The CubeSat can also be given a command in attitude and angular velocity in RPY frame.

#### 4.1.1 Kinematics Subsystem

The kinematics subsystem calculates the attitude of the CubeSat in body coordinates with respect to the RPY frame. Figure 4.2 shows the subsystem. It takes in the body rate of the CubeSat and integrates Equation 2.7.

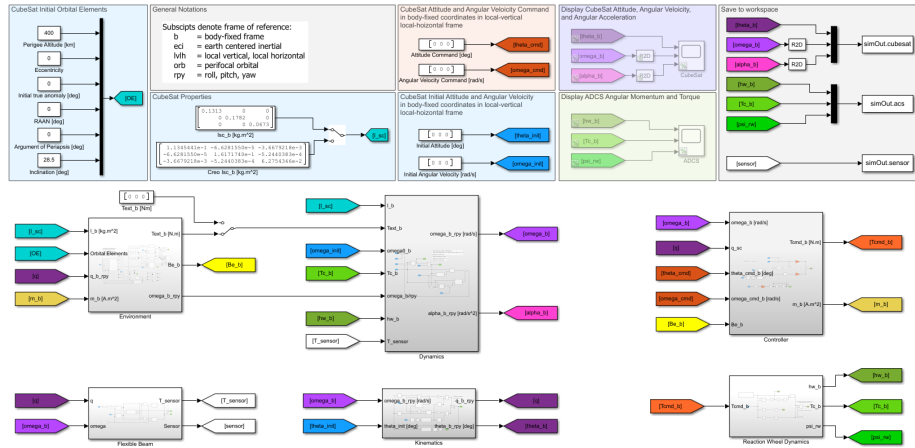


Figure 4.1: Top level of the attitude control simulation shows the initial orbital elements and satellite moment of inertia matrix configuration.

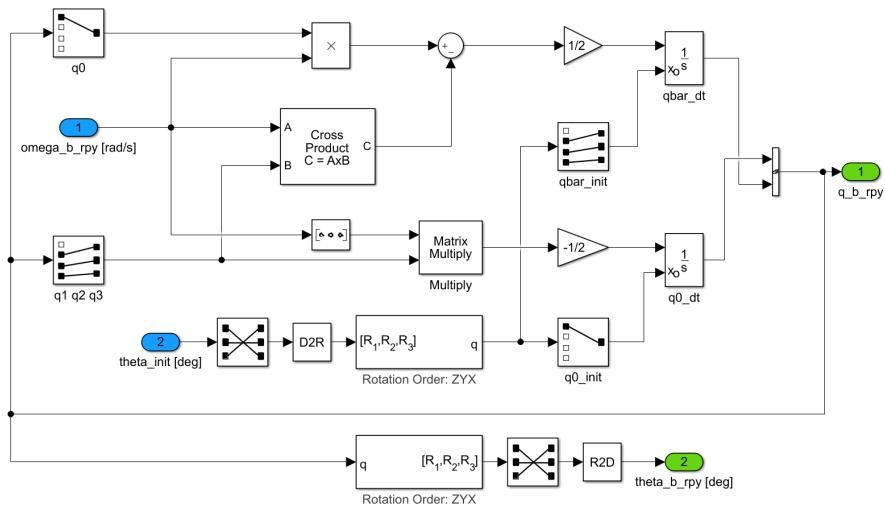


Figure 4.2: The kinematic subsystem calculates the attitude in body-fixed frame with respect to the RPY frame using the angular body rate.

### 4.1.2 Dynamics Subsystem

The dynamics subsystem calculates the body rate of the satellite by integrating the Euler rotational equation of motion. The equation of motion, Equation 2.10, must be modified to calculate the body rate in the RPY frame by including the rate of change of the orbital frame with respect to the ECI frame [21]. The local-vertical local horizontal (LVLH) rotates relative to the inertial frame of reference by a constant angular rate for a circular orbit. The rate is determined by the period of the orbit and can be calculated using Equation 4.1.

$$\omega_0 = \frac{2\pi}{P} \quad (4.1)$$

where the orbital period can be found for circular orbits using Equation 4.2.

$$P = \frac{2\pi}{\sqrt{\mu}} r^{3/2} \quad (4.2)$$

The LVLH rate of change with respect to the inertial frame can be written as a vector by  $\boldsymbol{\omega}_{lvlh} = [0, \omega_0, 0]^T$ . The LVLH can be converted to the RPY frame with a coordinate system transformation. The rotation matrix for the transformation from LVLH to RPY is constant and is shown in Equation 4.3.

$$C^{rpy/lvlh} = \begin{bmatrix} 0 & 1 & 0 \\ 0 & 0 & -1 \\ -1 & 0 & 0 \end{bmatrix} \quad (4.3)$$

The body angular rate in inertial frame of reference is the sum of the angular body rate in the RPY frame and the angular rate of the orbital frame given by



Equation 4.4.

$$\boldsymbol{\omega}_{eci} = \boldsymbol{\omega}_b + C^{b/rpy} \boldsymbol{\omega}_{rpy} \quad (4.4)$$

Taking the derivative of Equation 4.4 yields the following equation:

$$\dot{\boldsymbol{\omega}}_{eci} = \dot{\boldsymbol{\omega}}_b + \dot{C}^{b/rpy} \boldsymbol{\omega}_{rpy} + C^{b/rpy} \dot{\boldsymbol{\omega}}_{rpy} \quad (4.5)$$

For a circular orbit,  $\dot{\boldsymbol{\omega}}_{rpy} = 0$  and  $\dot{C}^{b/rpy} = -\boldsymbol{\omega}_b \times C^{b/rpy}$  so Equation 4.5 can be written as Equation 4.6.

$$\dot{\boldsymbol{\omega}}_{eci} = \dot{\boldsymbol{\omega}}_b - \boldsymbol{\omega}_b \times C^{b/rpy} \boldsymbol{\omega}_{rpy} \quad (4.6)$$

The total angular momentum of the satellite in the body frame can be written as the sum of the satellite and reaction wheel angular momentum:

$$\mathbf{H}_{tot} = \mathbf{H}_{sc} + \mathbf{h}_{rw} \quad (4.7)$$

where  $\mathbf{h}_{rw} = \mathbf{I}_{rw} \boldsymbol{\Omega}_{rw}$  is the moment of inertia matrix of the reaction wheels times the angular velocity of the reaction wheels. The reaction wheels are aligned to the body fixed coordinates which makes the MOI matrix a diagonal matrix as shown in Figure 4.8. The moment of inertia of each wheel is  $8.93 \cdot 10^{-5} \text{ kg} \cdot \text{m}^2$ .

$$\mathbf{I}_{rw} = \begin{bmatrix} I_{rw} & 0 & 0 \\ 0 & I_{rw} & 0 \\ 0 & 0 & I_{rw} \end{bmatrix} \quad (4.8)$$

Substituting Equation 4.7 into Equation 2.10, the spacecraft dynamics in the

inertial frame is written as:

$$\mathbf{I}\dot{\boldsymbol{\omega}}_{eci} + \dot{\mathbf{h}}_{rw} = -\boldsymbol{\omega}_{eci} \times (\mathbf{I}\boldsymbol{\omega}_{eci} + \mathbf{h}_{rw}) + \mathbf{T}_{ext} \quad (4.9)$$

The torque on the satellite by the reaction wheels is equal to the negative change in angular momentum of the reaction wheels [22].

$$\mathbf{T}_c = -\dot{\mathbf{h}}_{rw} \quad (4.10)$$

Inserting Equations 4.4, 4.6, and 4.10 into Equation 4.9 and using  $\boldsymbol{\omega}_{rpy}^b = C^{b/rpy}\boldsymbol{\omega}_{rpy}$ , the dynamics of the CubeSat can be written as

$$\mathbf{I}\dot{\boldsymbol{\omega}}_b = \mathbf{I}\boldsymbol{\omega}_b \times \boldsymbol{\omega}_{rpy}^b - (\boldsymbol{\omega}_b + \boldsymbol{\omega}_{rpy}^b) \times [\mathbf{I}(\boldsymbol{\omega}_b + \boldsymbol{\omega}_{rpy}^b) + \mathbf{I}_{rw}\boldsymbol{\Omega}_{rw}] + \mathbf{T}_c + \mathbf{T}_{ext} \quad (4.11)$$

The Simulink subsystem integrates Equation 4.11 using the initial conditions specified and using the angular momentum and control torque from the ACS. The model is shown in Figure 4.3.

37

### 4.1.3 Controller and Reaction Wheel Subsystems

A Proportion-Derivative (PD) controller was chose as it is asymptotically stable and easy to implement [2]. The proportional gain was on the attitude error vector and the derivative gain was on the angular rate error vector.

$$\mathbf{u} = -k_p \mathbf{q}_e - k_d \boldsymbol{\omega}_e \quad (4.12)$$

where the attitude error is given by the quaternion rotation shown in Equation 4.13.

$$\mathbf{q}_e = \mathbf{q}_c^{-1} \mathbf{q}_T \quad (4.13)$$

The control law gives the commanded torque to the reaction wheel assembly. If it was an ideal ACS then the commanded torque would equal the torque output of the reaction wheels. However, the reaction wheels must spin up or down to meet the torque demand by the controller which introduce more dynamics into the system. The simulation has the option to select whether or not to implement the idealized control torque where the control toque is applied instantaneously or to simulate the reaction wheel dynamics. In the latter case, the torque demand from the controller is used to calculate the acceleration of the reaction wheel since the torque of the reaction wheels is equal to its moment of inertia matrix times its angular acceleration. Taking the product of the inverse MOI and the commanded torque, the angular acceleration is found. It integrated and based through saturation blocks based on the MAI-400 specifications to obtain the angular velocity of the reaction wheels. The product of the MOI matrix and the angular velocity of the reaction wheels gives the angular momentum of the reaction wheel assembly [23].

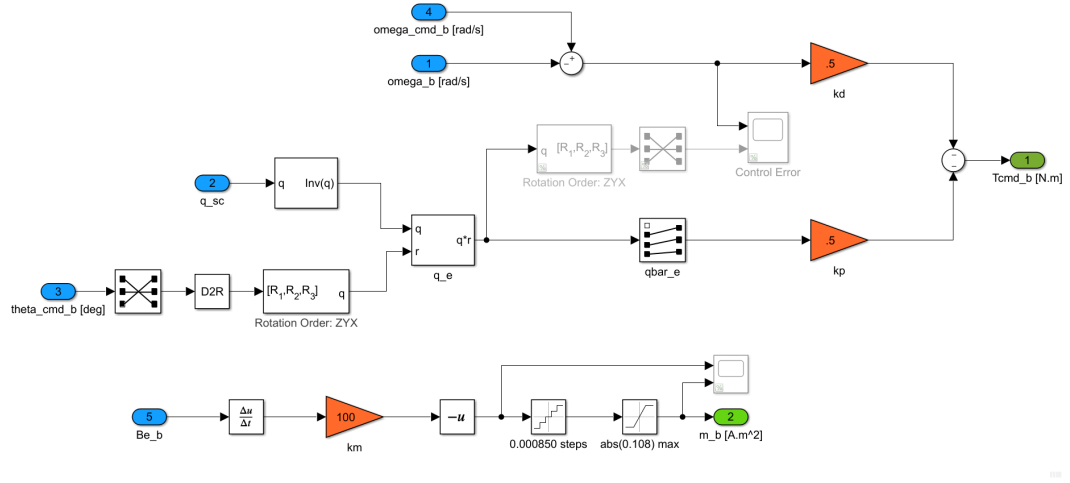


Figure 4.4: The controller subsystem calculates the control torque demand based on a PD controller with quaternion and body-rate feedback.

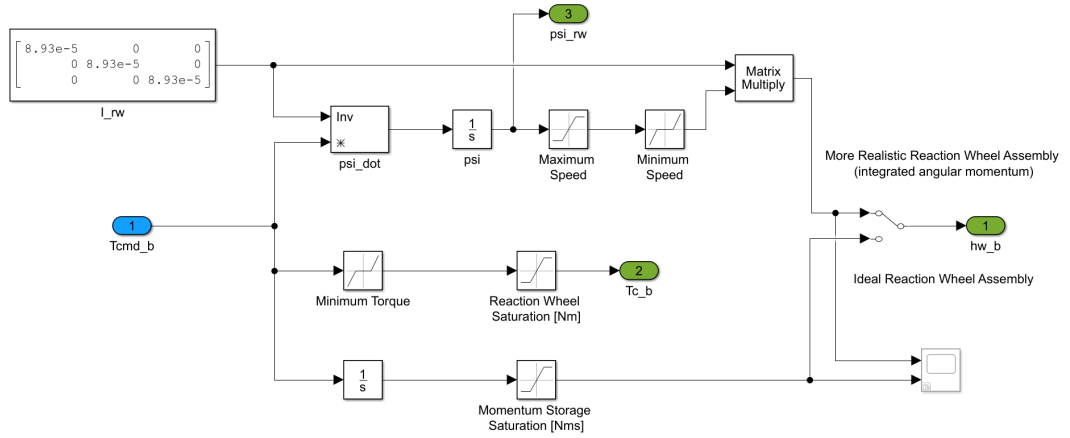
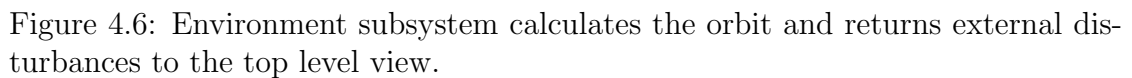


Figure 4.5: Reaction wheel dynamics subsystem calculates the output torque based on the torque demand provided by the controller.

This Simulink block calculates the orbit of the CubeSat and the environmental disturbances that the CubeSat will experience along the orbit. The block on the left in Figure 4.6 takes the orbital elements specified and calculates the orbit in inertial coordinates. The orbit is used for visual reference. The four blocks on the right side of the figure calculate the environmental torques in body-fixed frame using the current spacecraft attitude.



40

Table 4.1: Orbital elements used in the simulation.

Element	Symbol	Value	Unit
Semi-major axis	$a$	6778	km
Eccentricity	$e$	0	
Inclination	$i$	28.5	deg
Longitude of the Ascending Node	$\Omega$	0	deg
Argument of Periapsis	$\omega$	0	deg
True Anomaly	$\theta$	0	deg

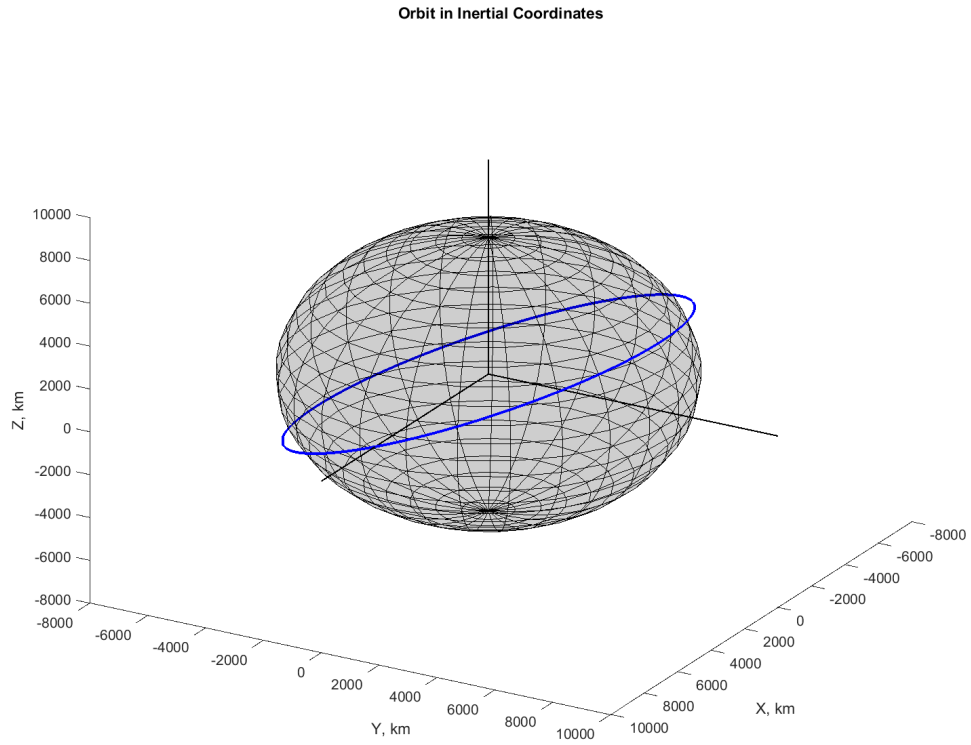


Figure 4.7: The 400 km circular orbit with a 28.5 deg inclination.

### 4.1.5 Sensor Subsystem

This block calculates the sensor position relative to the RPY frame and calculates the effective internal torque on the spacecraft to couple the motion of the CubeSat and sensor. The sensor was modeled as a simplified lumped mass model in 3 dimension. The three dimensions were all translation in the body-fixed coordinate system with respect to the RPY frame. The sensor's motion is modeled as a mass-spring-damper and included the mass of the bracket and boom. The equation of motion for a mass-spring-damper is given by

$$m\ddot{x} + c\dot{x} + kx = 0 \quad (4.14)$$

Since the motion of the boom impacts the motion of the satellite, the motion of the two are coupled. The equations of motion of the sensor for the coupled beam and sensor mass is given by:

$$m\ddot{x} + c(\dot{x} - L\dot{\theta}) + k(x - L\theta) = 0 \quad (4.15)$$

where  $m$  is the mass of the sensor, bracket, and boom,  $c$  is the damping coefficient of the sensor, bracket and boom, and  $k$  is the spring constant of the assembly. The spring constant was found by using the fundamental frequency from the modal analysis and the mass of the assembly. The spring constant can be calculated using

$$k = m\omega_n^2 \quad (4.16)$$

where  $\omega_n$  is the first fundamental frequency of the boom. The dynamics equa-



tion of motion of the spacecraft with the effects of the boom is given below:

$$I\ddot{\theta} + cL(L\dot{\theta} - \dot{x}) + kL(L\theta - x) = f(\theta) \quad (4.17)$$

where  $f(\theta)$  is right side of Equation 4.11. The Simulink model of the sensor equation of motion is shown in Figure 4.8. The coupled equations of motion in matrix form is given below:

$$\begin{bmatrix} I & 0 \\ 0 & m \end{bmatrix} \begin{Bmatrix} \ddot{\theta} \\ \ddot{x} \end{Bmatrix} + \begin{bmatrix} cL^2 & -cL \\ -cL & c \end{bmatrix} \begin{Bmatrix} \dot{\theta} \\ \dot{x} \end{Bmatrix} + \begin{bmatrix} kL^2 & -kL \\ -kL & k \end{bmatrix} \begin{Bmatrix} \theta \\ x \end{Bmatrix} = \begin{Bmatrix} f(\theta) \\ 0 \end{Bmatrix} \quad (4.18)$$

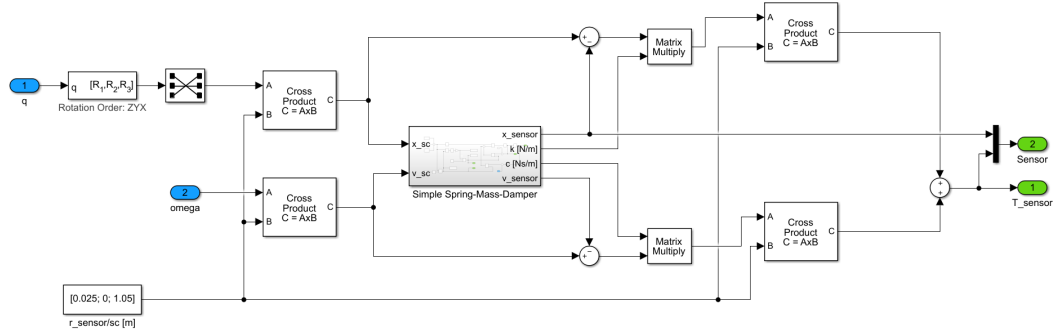


Figure 4.8: Sensor subsystem calculates the sensor position and internal torque on the CubeSat.

## 4.2 Structural Simulations

The structural analysis was performed using ANSYS Workbench 2018. The boom and bracket was modeled using Creo Parametric and imported into ANSYS as a step file. A modal analysis was performed to find the fundamental frequencies to determine the impact it will have on control system.

### 4.2.1 Modal Analysis

A modal analysis was performed on the boom to determine the fundamental frequencies and the corresponding mode shapes. Since the boom has a thickness of 0.23 mm and a length of 1 m, there was concern regarding coupling between the boom and control system response to environmental disturbances and commanded attitudes. The beam was modeled as a surface geometry and a sensor attachment bracket was modeled as a solid to provide some torsional stiffness. The beam was prescribed a thickness of 0.23 mm and the material properties for the composite were provided by Rocco. The material used for the bracket was aluminum alloy. A distributed mass of 30g was applied to the surface on the bracket facing away from the CubeSat in the z-axis to represent the sensor. The sensor module was not modeled since was considered a rigid-body with respect to the boom. A fixed support is applied to the other end of the beam. It was assumed that the fixed support boundary condition represented the realistic boundary condition for the assembly. In reality, the boom is not fixed to a surface, there is a section of the beam where it flattens out to be rolled up. It would be constrained from moving in the axial direction by either strain energy or by the motor used to deploy the boom. The housing would constrain it in the other two axis as well as any rotations

at the base. The transition section is not modeled in this analysis and is out of the scope of this thesis. A complete model setup is shown in Figure 4.9

The first 6 modes were determined in ANSYS. Figure 4.10 shows the mesh generated which consisted of 14,709 nodes and 4,530 elements. The mesh used shell elements for the beam geometry and solid elements for the sensor bracket. Quality of the mesh was measured by the ANSYS metric skewness. Skewness is a measure of how close a face or cell is to the ideal shape which would be an equilateral or equiangular shape depending on the type of element. The average skewness of an element in the generated mesh was 0.144 with a standard deviation of 0.175. A skewness value below 0.25 indicates excellent quality and most elements in the mesh fall within this category. The quality distribution of the mesh is shown in Figure 4.11. Therefore, the results of the modal analysis are accurate as modeled and there are no degenerate elements that could cause numerical errors in the solution.

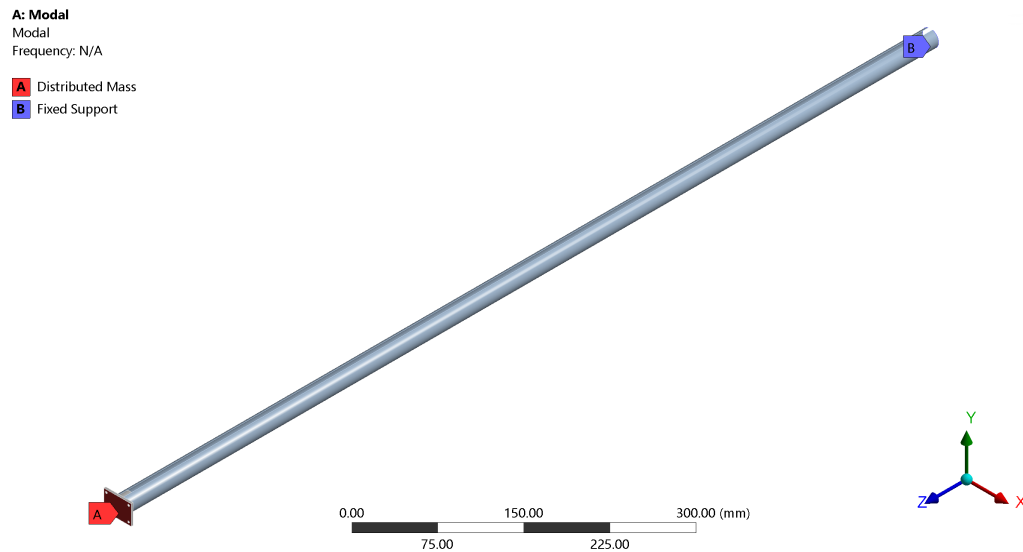


Figure 4.9: Modal analysis setup

Mesh

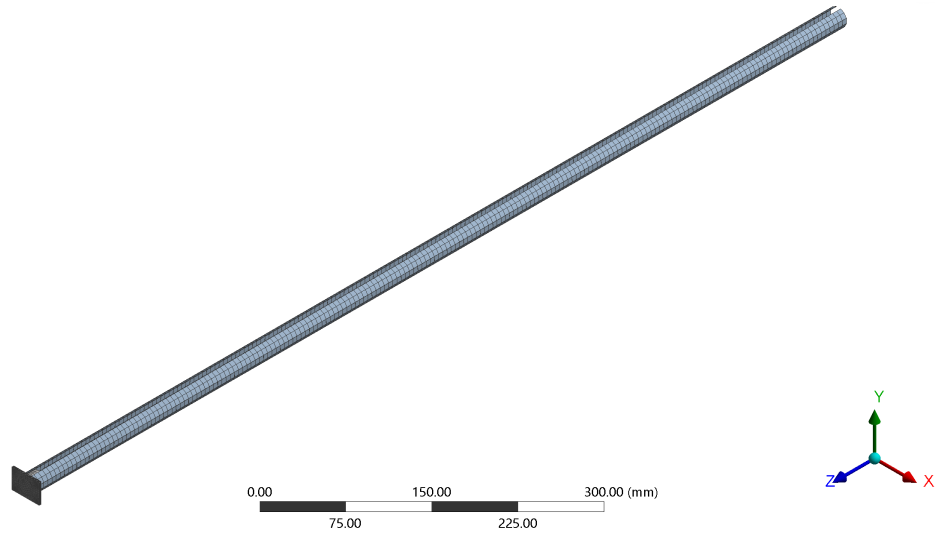


Figure 4.10: Modal analysis generated mesh.

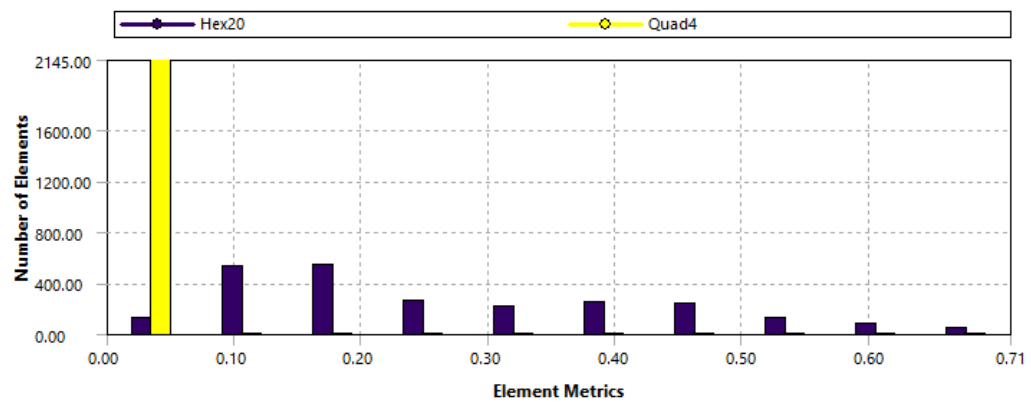


Figure 4.11: The element skewness distribution of the mesh.

# Chapter 5

## Results

### 5.1 Structural Simulations

The modal analysis performed in ANSYS Workbench yielded the first 6 fundamental frequencies and mode shapes of the sensor and boom assembly. The results from the modal analysis were used to determine the equivalent spring constant of the sensor and boom assembly. It also provided insight on how to model the beam and sensor for the attitude control simulation.

#### 5.1.1 Modal Analysis

The ANSYS modal analysis showed that the first 2 natural frequencies occurred below 10Hz. These low frequencies could be easily excited by the rigid-body modes of the CubeSat or by the actuation of the reaction wheels. The natural frequencies and corresponding mode shapes determined by ANSYS are listed in Table 5.1. The incorporation of the sensor bracket at the free end of the boom increased the

torsional stiffness of the boom. Without the bracket, the free-end of the boom was allowed to deform. For the first few mode shapes, torsion was present. To better capture the design of the boom and sensor, the bracket was added. This removed torsion from the first 2 mode shapes and increased the natural frequencies as well. The first mode shape represented a bending mode in the y-axis as seen in Figure 5.1 and had a corresponding natural frequency of 6.70Hz. The second mode represented a bending mode in the x-axis as seen in Figure 5.2 with a natural frequency of 7.35Hz. The following natural frequencies were an order of magnitude higher than the first 2. Therefore, the first and second mode shapes and corresponding natural frequencies are the focus of further coupled dynamics between the spacecraft and boom/sensor assembly.

Table 5.1: Summary of modal frequencies and shapes

<b>Mode</b>	<b>Frequency [Hz]</b>	<b>Shape</b>
1	6.7027	Bending
2	7.3519	Bending
3	37.378	Bending/Torsion
4	64.057	Bending
5	99.782	Bending/Torsion
6	161.82	Torsion

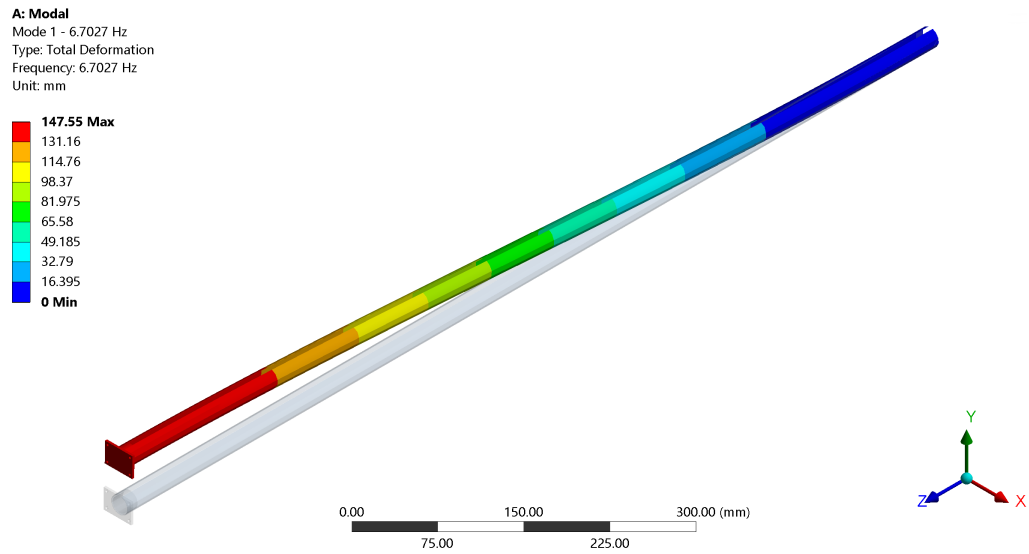


Figure 5.1: First mode shape of the payload was a bending mode in the y-axis (vertical) at a frequency of 6.70 Hz.

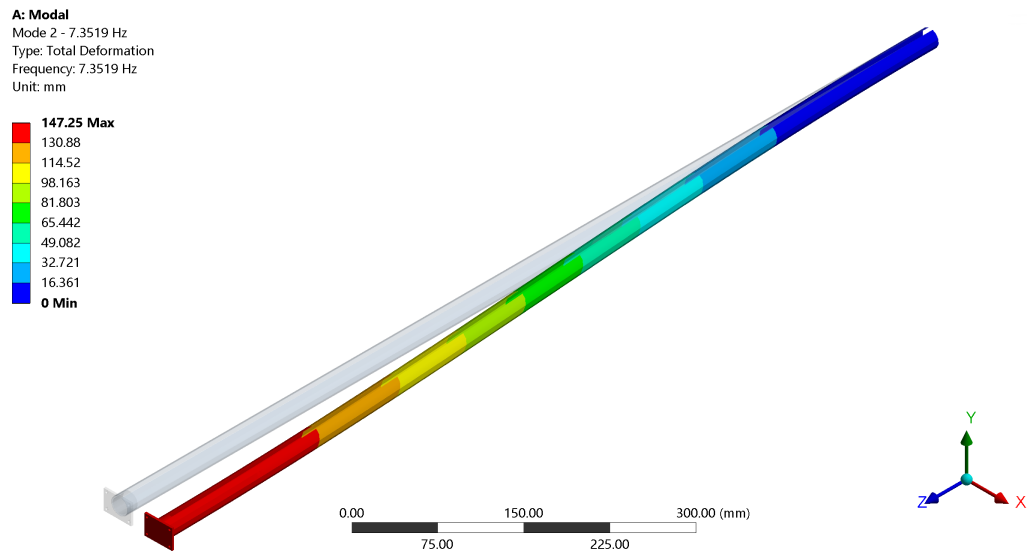


Figure 5.2: Second mode shape of the payload was a bending mode in the x-axis (horizontal) at a frequency of 7.35 Hz.

## 5.2 Attitude Control System

The attitude control system was tested for maintaining the spacecraft and boom/sensor assembly (the satellite) in a nadir-pointing attitude while under the influence of the environmental disturbances described in Chapter 2 and modeled in Chapter 4. The simulation was run with zeroed initial conditions meaning there was no initial attitude offset nor any commanded angular body-rate for the satellite. The simulation was performed over one orbit to determine the response of the satellite from the total environmental disturbances modeled.

### 5.2.1 CubeSat Response

The CubeSat was able to handle the environmental disturbances as well as the response of the flexible boom and sensor to hold nadir within  $\pm 0.5^\circ$  with a proportional gain of 0.43 and derivative gain of 0.4 for the controller. Increasing the gain leads to quicker saturation of the momentum wheels but improved pointing performance. By increasing the gains, the CubeSat can maintain pointing within a specified error. The CubeSat's response time history can be seen in Figure 5.3. The change in attitude of the CubeSat is enough to cause saturation of the angular momentum in the reaction wheels as seen in Figure 5.4. Momentum dumping of the reaction wheels using the magnetorquers will need to be implemented in order to accommodate the addition of the flexible boom/sensor assembly. The equivalent torque produced by the payload was several orders of magnitude larger than the torque from the environmental disturbances. Therefore, the response of the CubeSat is dominated by the dynamics of the boom and sensor assembly.



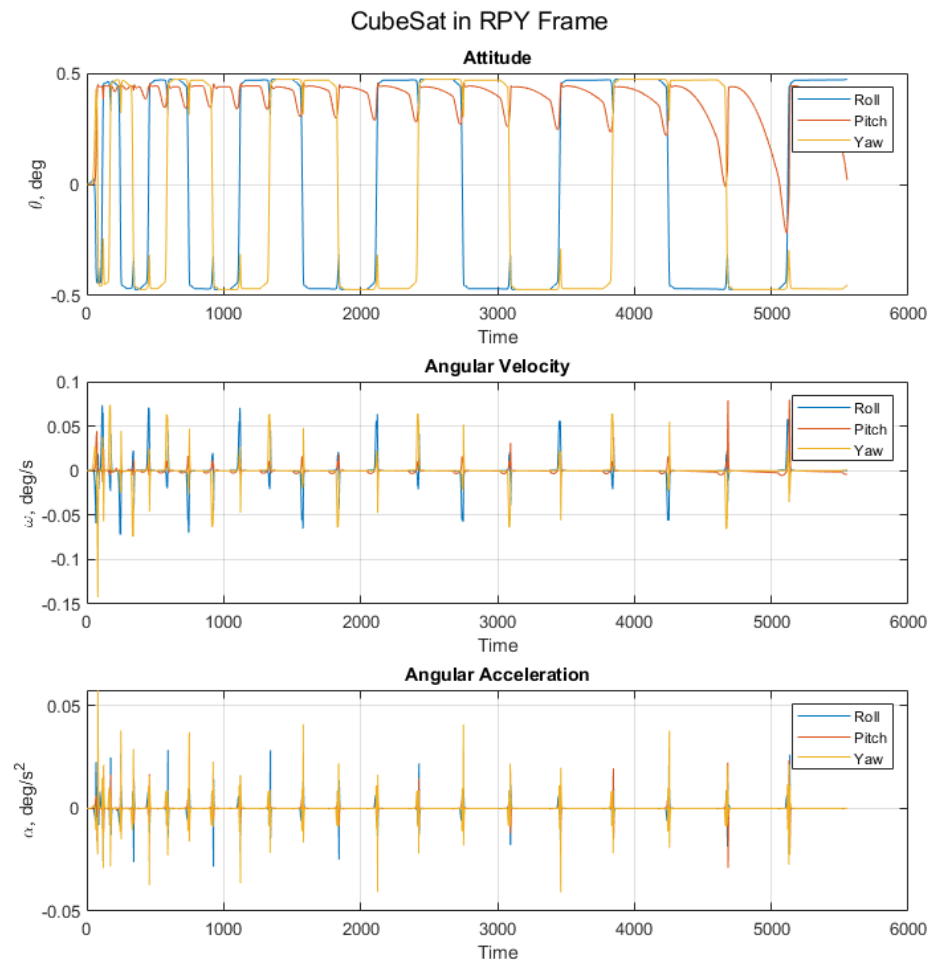


Figure 5.3: CubeSat attitude, angular velocity, and angular acceleration.

### 5.2.2 ADACS Response

The simulation showed the ADACS is saturated with angular momentum with the reaction wheels operating at maximum speed. The time history of the torque output, angular momentum, and angular velocity of the reaction wheels is shown in Figure 5.4. For the ADACS to respond quickly to the disturbances and keep the CubeSat oriented with a tight margin, the wheels become saturated. A momentum dumping scheme will have to be implemented or the requirements on the pointing error will have to be relaxed. The pitch axis becomes saturated very early in the orbit but does not oscillate like the other two reaction wheels. This is due in large part to the sensor and boom payload response and the almost constant disturbance in the pitch axis due to the gravity gradient and the aerodynamic drag. The payload is least stiff in the transverse directions to the boom which can cause a torque about the pitch or roll axis. Since the disturbances mainly cause a torque about the pitch axis, the payload responds with an oscillation about that axis. This also creates a torque that the ADACS will have to counteract.

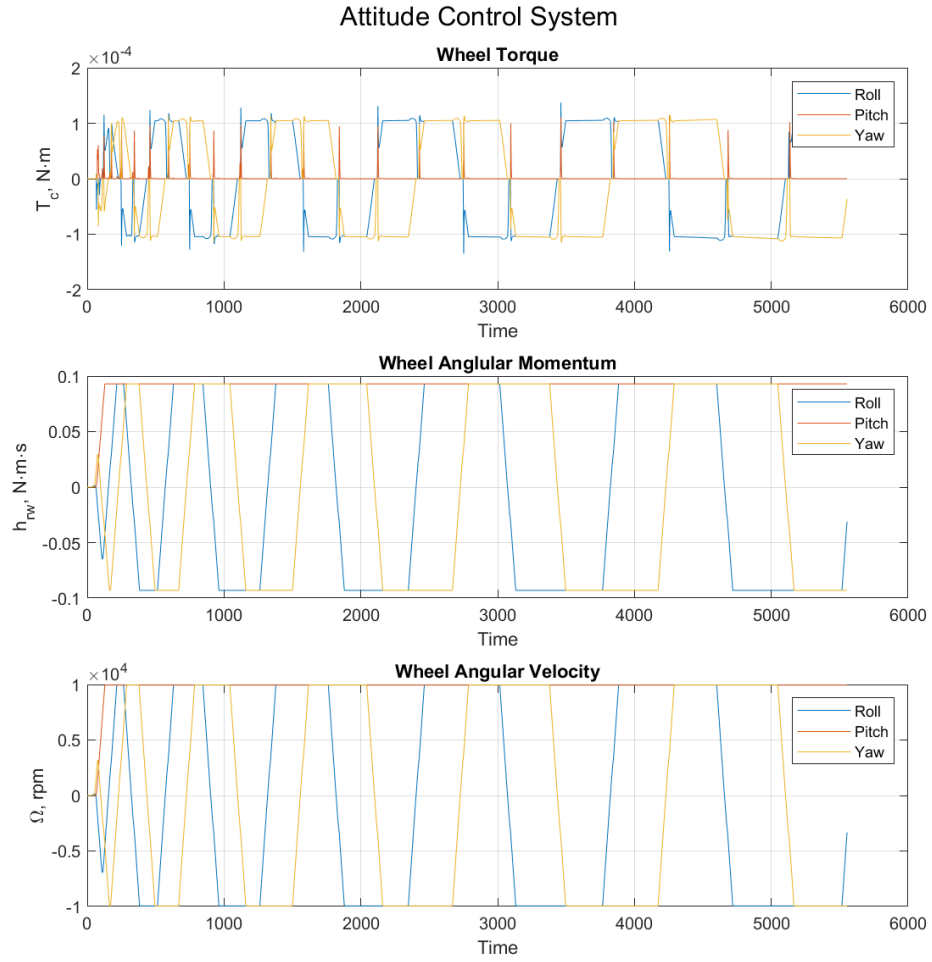


Figure 5.4: Attitude control system response to environmental disturbances and internal torque from the sensor mass.

### 5.2.3 Sensor Response

The sensor was able to settle quickly to the excitation from the ADACS with a prescribed damping ratio of 0.1. A low damping ratio was chosen to add some damping to the boom in the interest of realism, however the actual damping in the system should be determined from experimental methods. Determination of the effective damping ratio for the boom / sensor assembly was outside the scope of this research. The maximum displacement seen was in the roll axis which was expected due to the aerodynamic torque. The maximum displacement seen was -0.09mm and the time history of all axis is shown in Figure 5.5. The torque from the sensor to the spacecraft was several orders of magnitude larger than the magnitudes associated with the environmental torques as seen in Figure 5.6. Therefore, the response of the CubeSat is influenced significantly by the dynamics associated with the boom and sensor assembly.

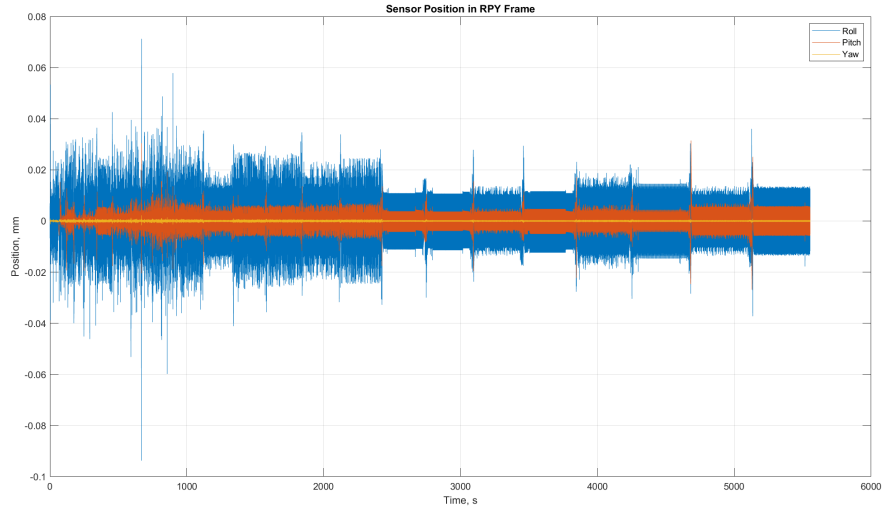


Figure 5.5

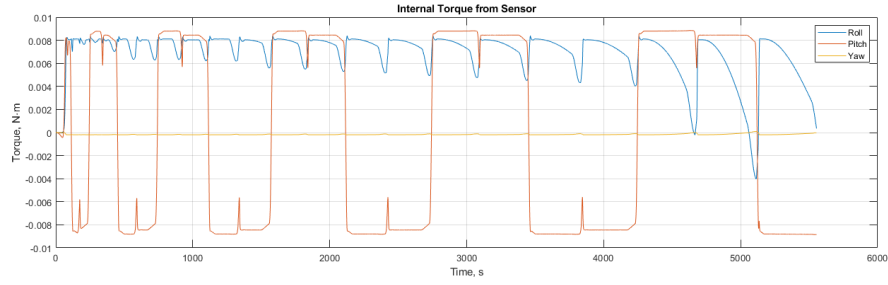


Figure 5.6: Sensor response to the attitude control system for nadir pointing.

### 5.2.4 Environmental Disturbances

All the environmental disturbances modeled were comparable. It is shown from Figure 5.7 that the environmental disturbances produce an almost constant torque about the pitch axis. While the solar pressure disturbance had the highest magnitude, it was only applied for half the orbit due to the satellite being shielded while in Earth's umbra. The larger torque for the solar pressure is because of the larger surface area from the solar array versus the surface area of only the 3U or 6U side facing the velocity vector. The surface area used for the aerodynamic drag is about 3,000 cm<sup>2</sup> or 6,000 cm<sup>2</sup> depending on which side is facing the direction along the velocity vector. This is compared to the 20,000cm<sup>2</sup> from which the solar array makes up most of the surface area that is facing the sun vector. The gravity gradient torque shows the torque about the pitch axis as expected. The torque produced by the gravity gradient is directed normal to the orbital plane. Due to the other disturbances changing the attitude of the CubeSat, it experienced torques about the other two body axis instead of a constant torque about the pitch axis.

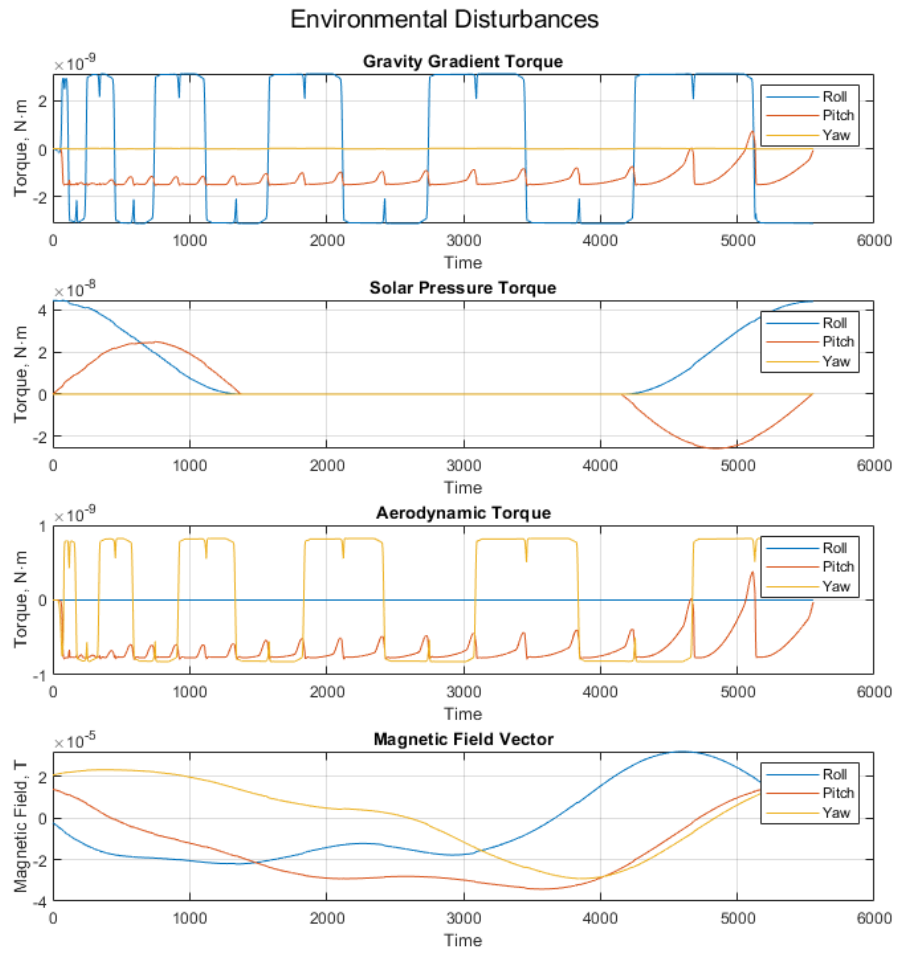


Figure 5.7: Environmental disturbance over one orbit.

# Chapter 6

## Conclusion

### 6.1 Summary

An attitude control system was modeled in Simulink for a 6U CubeSat with a sensor attached to a flexible boom. The control system was shown to be able to handle the modeled environmental disturbances and was shown to hold the CubeSat within  $\pm 0.5$  deg although at the cost of saturating the ADACS. To achieve the tight pointing error, high gains were used for the controller. Relaxing the requirements on the attitude error could result in better performance from the ADACS by keeping the response below the saturation levels of the reaction wheels. The response of the payload showed small displacements of the payload as modeled as a simple mass-spring-damper. More accurate modeling of the payload will further improve the accuracy of the simulation and provide better insight into the response of the system.

## 6.2 Discussion

Much time was spent modeling and debugging the attitude control model. Minor errors were hard to find and often went unnoticed for a period of time. They often don't lead to the solution becoming unstable or other recognizable signs. One of the most important things learned in modeling is to document the model carefully and clearly. Another important lesson learned is to pay close attention to the frame of reference not only in my simulation but in other papers as well. Modeling is very important not only on the accuracy of the solution but also the time and computational resources required to solve it. Tradeoffs between the two need to be carefully considered to determine what and how detailed to include in a model.

## 6.3 Future Work

The simulation has a few areas which can be improved upon. The controller gain selection can be improved upon. Other methods based on optimal gain such as LQR and  $H_\infty$  methods for the nonlinear system will improve the response of the satellite. Additionally, custom slewing profiles which focus on minimizing the torque to the beam could be implemented if maximum performance by the ADACS is not a necessity. One area will have the most impact on the simulation and future testing which would be better modeling of the beam. This could include running the simulation simultaneously with a FEM model or using continuous beam equations in the model. This would give a more accurate response of the beam and the equivalent impact on the CubeSat.

Then the next step would be to test the simulation with a hardware in the loop test of the MAI-400. By simulating the response of the CubeSat and sensor



payload, the ADACS could be tested to see if the MAI-400 could provide the torque commanded by the controller. The controller in the simulation can be fine-tuned to incorporate a more realistic response from the ADACS. This would improve the simulation accuracy and allow for easy analysis for design changes. A structural analysis of the boom and sensor assembly and an accompanying test for validation of the structural model is needed to determine if the boom will handle the response from the ADACS. A transient structural FEM could be modeled in ANSYS Workbench. The time history of the CubeSat can be exported and used as the input to the structural model. Testing a physical model would be a difficult task as it would require simulating a zero-gravity environment. Testing would likely have to be divided to test in one axis at a time.

# References

- [1] J. Deaton. How cubesats are changing the way we use satellites. [Online]. Available: <https://www.linkedin.com/pulse/cubesats-101-what-going-up-juan-d-deaton-ph-d->
- [2] A. H. de Ruiter, C. J. Damaren, and J. R. Forbes, *Spacecraft Dynamics and Control*. John Wiley & Sons, Inc., 2013.
- [3] J. Bido, “System study of an on-orbit additive manufacturing cubesat,” Master’s thesis, Florida Institute of Technology, 2017.
- [4] *6U CubeSat Design Specification Rev. 1.0*, The CubeSat Program, Cal Poly SLO, Jun. 2018.
- [5] A. Poghosyan and A. Golkar, “Cubesat evolution: Analyzing cubesat capabilities for conducting science missions,” *Progress in Aerospace Sciences*, vol. 88, pp. 59–83, Jan.
- [6] X. Xia, G. Sun, Z. Keke, S. Wu, T. Wang, L. Xia, and S. Liu, “Nanosat-s/cubesats adcs survey,” in *2017 29th Chinese Control And Decision Conference (CCDC)*. IEEE, May 2017, pp. 5151–5158.

- [7] J. R. Wertz, *Spacecraft Attitude Determination and Control*. Microcosm, Inc., 1999.
- [8] F. Davoli, C. Kourogiorgas, M. Marchese, A. Panagopoulos, and F. Patrone, “Small satellites and cubesats: Survey of structures, architectures, and protocols,” *International Journal of Satellite Communications and Networking*, vol. 37, no. 4, pp. 343–359, Jul. 2019.
- [9] *State of the Art Small Spacecraft Technology*, NASA, Dec. 2018.
- [10] D. Selva and D. Krejci, “A survey and assessment of the capabilities of cubesats for earth observation,” *Acta Astronautica*, vol. 74, pp. 50–68, May 2012.
- [11] S. A. Rawashdeh and J. E. Lumpp, “Aerodynamic stability for cubesats at iss orbit,” *Journal of Small Satellites*, vol. 2, no. 1, pp. 85–104, 2013.
- [12] H. Curtis, *Orbital Mechanics for Engineering Students*. Elsevier Ltd., 2014.
- [13] S. Rao, *Mechanical Vibrations*, 5th ed. Prentice Hall, 2010.
- [14] H.-H. Lee, *Finite Element Simulations with ANSYS Workbench 18*. SDC Publications, 2018.
- [15] *6U SUPERNOVA Payload Interface Control Document (ICD)*, Pumpkin Inc., 2014.
- [16] *SUPERNOVA BM2/MAI-400 Bus*, Pumpkin Inc., 2016.
- [17] *SUPERNOVA Payload Interface Control Document (ICD)*, Pumpkin Inc., 2017.
- [18] *MAI-400 1/2U CubeSat ADACS*, Maryland Aerospace Inc.

- [19] D. Turse, *Roccor Deployable Instrument Boom Technology Overview Provided to Florida Institute of Technology*, Roccor Inc., 2018.
- [20] *Laser Pumped Cesium Magnetometer*, Geometrics Inc., 2017.
- [21] Y. Yang, “Spacecraft attitude determination and control: Quaternion based method,” *Annual Reviews in Control*, vol. 36, no. 2, pp. 198–219, Dec. 2012.
- [22] —, “Spacecraft attitude and reaction wheel desaturation combined control method,” *IEEE Transactions on Aerospace and Electronic Systems*, vol. 53, no. 1, pp. 286–295, 2017.
- [23] E. Dannemeyer, “Design and analysis of an attitude determination and control subsystem (adcs) for afit’s 6u standard bus,” Ph.D. dissertation, Air Force Institute of Technology, Mar. 2014.
- [24] F. Beer, Jr., E. Johnston, J. DeWolf, and D. Mazurek, *Mechanics of Materials*, 7th ed. McGraw-Hill Education, 2014.

# Appendix

## Flexible Beam Mode Shapes

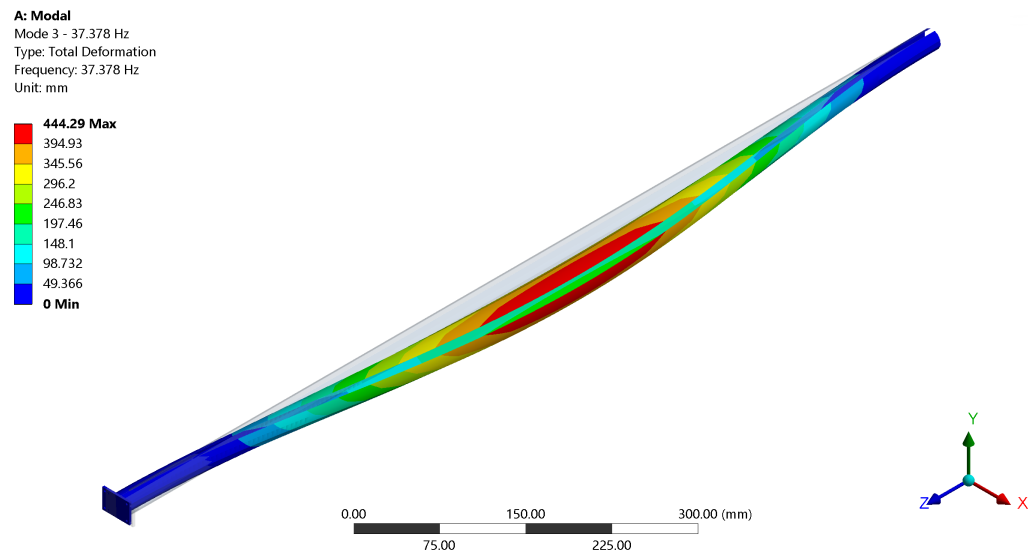


Figure 1: Mode shape for the 3rd natural frequency is a bending and torsion mode.

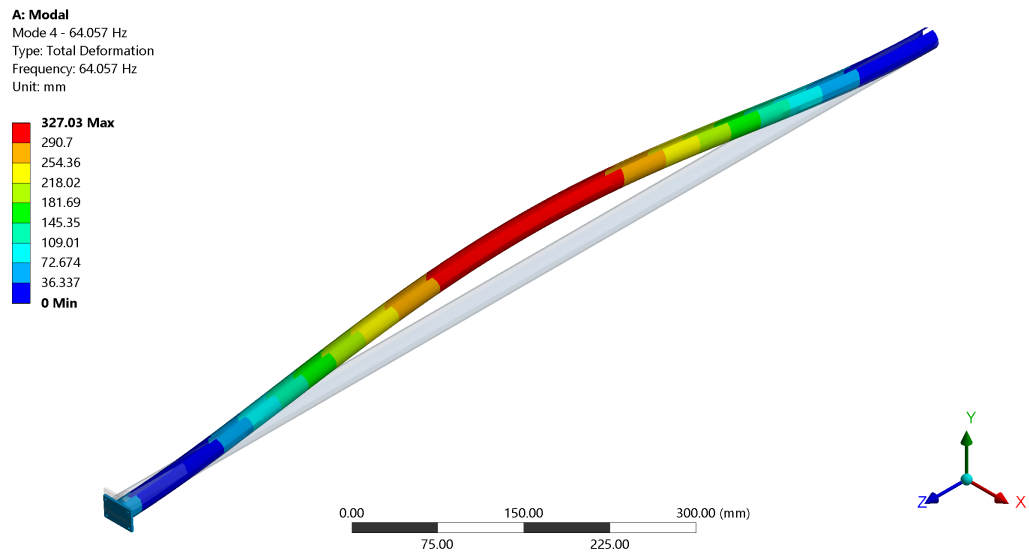


Figure 2: Mode shape for the 4th natural frequency is a bending mode.

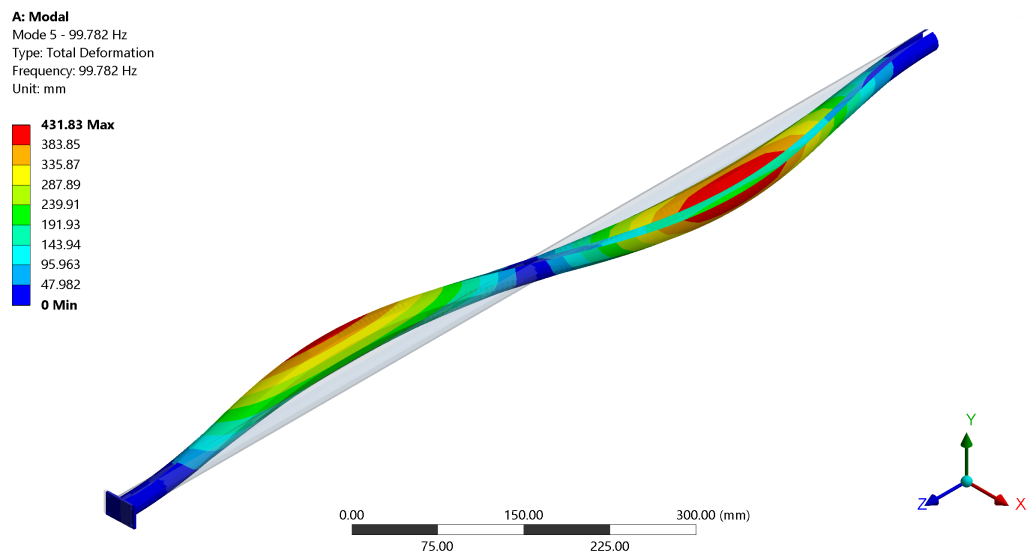


Figure 3: Mode shape for the 5th natural frequency is a bending and torsion mode.

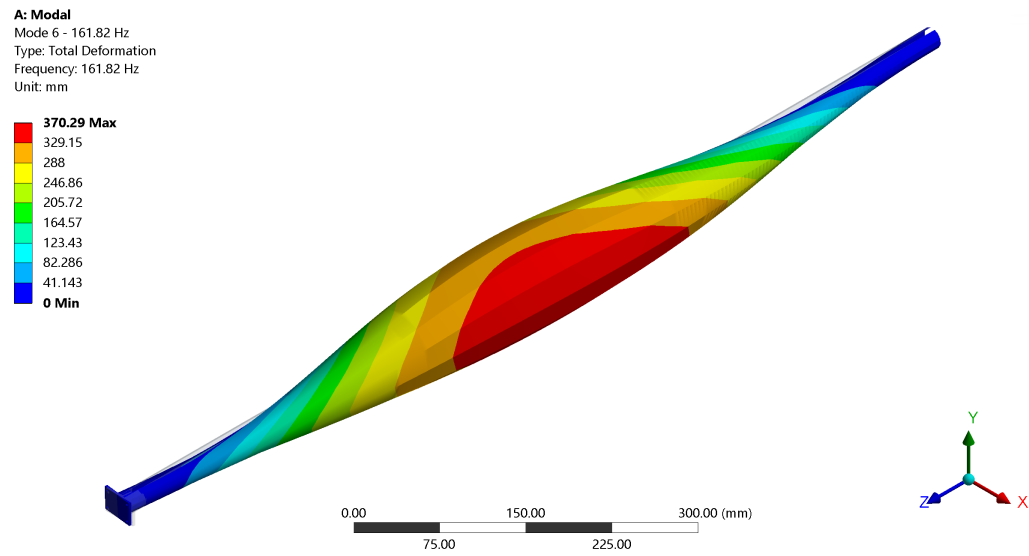


Figure 4: Mode shape for the 6th natural frequency is a torsion mode about the z-axis.